

ESPRESSO observations of HE 0107–5240 and other CEMP-no stars with $[\text{Fe}/\text{H}] \leq -4.5$ [★]

D. S. Aguado^{1,2} ^{★★}, P. Molaro^{3,4}, E. Caffau⁵, J. I. González Hernández^{6,7}, M. R. Zapatero Osorio⁸, P. Bonifacio⁵, C. Allende Prieto^{6,7}, R. Rebolo^{6,7,9}, M. Damasso¹⁰, A. Suárez Mascareño^{6,7}, S. B. Howell¹¹, E. Furlan¹², S. Cristiani³, G. Cupani³, P. Di Marcantonio³, V. D’Odorico^{3,13,4}, C. Lovis²⁰, C. J. A. P. Martins^{15,16}, D. Milakovic¹⁷, M. T. Murphy¹⁸, N. J. Nunes¹⁴, F. Pepe²⁰, N. C. Santos^{21,22}, T. M. Schmidt^{3,19}, A. Sozzetti¹⁰

(Affiliations can be found after the references)

October 12, 2022

ABSTRACT

Context. HE 0107–5240 is a hyper metal-poor star with $[\text{Fe}/\text{H}] = -5.39$, one of the lowest-metallicity stars known. Its stellar atmosphere is enhanced in carbon, with $[\text{C}/\text{Fe}] = +4.0$, without detectable presence of neutron-capture elements. Therefore, it belongs to the Carbon-Enhanced Metal-Poor (CEMP-*no*) group as the majority of most metal-poor stars known to date. Recent studies showed variations in the line-of-sight velocity of HE 0107–5240, suggesting it belongs to a binary system. CEMP-*no* stars are the closest descendants of the very first Pop III stars and binarity holds important bearings for the poorly known mechanism leading to their formation.

Aims. We performed high-resolution observations with the ESPRESSO spectrograph at the VLT to constrain the kinematical properties of the binary system HE 0107–5240 and to probe the binarity of the sample of 8 most metal-poor stars with $[\text{Fe}/\text{H}] \leq -4.5$.

Methods. Radial velocities are obtained by using cross-correlation in the interval 4200–4315 Å, which contains the relatively strong CH band, against a template that could be either a synthetic spectrum or a combined observed spectrum in an iterative process. A Bayesian method is applied to calculate the orbit by using the ESPRESSO measurements and others from the literature. Chemical analysis has also been performed in HE 0107–5240 employing spectral synthesis with the SYNTHÉ and ATLAS codes.

Results. Observations of HE 0107–5240 spanning more than 3 years show a monotonic decreasing trend in radial velocity at a rate of approximately by $0.5 \text{ m s}^{-1} \text{ d}^{-1}$. A maximum v_{rad} was reached between March 13th, 2012, and December 8th, 2014. The period is constrained at $P_{\text{orb}} = 13009^{+1496}_{-1370} \text{ d}$. New more stringent upper limits have been found for several elements: a) $[\text{Sr}/\text{Fe}]$ and $[\text{Ba}/\text{Fe}]$ are lower than -0.76 and $+0.2$ respectively, confirming the star is a CEMP-*no*; b) $A(\text{Li}) < 0.5$ is well below the plateau at $A(\text{Li}) = 1.1$ found in the Lower Red Giant Branch stars, suggesting Li was originally depleted; and c) the isotopic ratio $^{12}\text{C}/^{13}\text{C}$ is 87 ± 6 showing very low ^{13}C in contrast to what expected from a *spinstar* progenitor.

Conclusions. We confirm that HE 0107–5240 is a binary star with a long period of about 13000 d (~ 36 years). The carbon isotopic ratio excludes the possibility that the companion has gone through the AGB phase and transferred mass to the currently observed star. The binarity of HE 0107–5240 implies some of the first generations of low-mass stars form in multiple systems and indicates that the low metallicity does not preclude the formation of binaries. Finally, a solid indication of v_{rad} variation has been found also in SMSS 1605–1443.

Key words. binaries: spectroscopic – stars: abundances – stars: Population II – stars: Population III – Galaxy: abundances – Galaxy: formation – Galaxy: halo

1. Introduction

HE 0107–5240 is a hyper metal-poorⁱ star discovered in the context of the Hamburg/ESO survey (Christlieb et al. 2001) first reported by Christlieb et al. (2002a). HE 0107–5240 shows carbon enhancement of $[\text{C}/\text{Fe}] = +4.0$ but with no significant n-capture elements enrichment. Therefore, it belongs to the class of the carbon-enhanced metal-poor star called CEMP-*no*, that is $[\text{C}/\text{Fe}] > 1$ and $[\text{Ba}/\text{Fe}] < 0$ (Beers & Christlieb 2005). Two years later Frebel et al. (2005) found a very similar star, HE 1327–2326 with $[\text{Fe}/\text{H}] = -5.6$, which prompted a discussion on the frequency of these extremely rare objects (see Cayrel 2005). So far, 14 stars with metallicities $[\text{Fe}/\text{H}] < -4.5$ are known. These stars are the objects with the lowest metallicity measured in primitive Pop II stars and provide insight into the

nature of the First Stars and on the first chemical production. The iron abundance of these stars is so low that only a few progenitors, possibly even only one, polluted the gas out of which they were formed. The carbon enhancement has been explained by the explosion of faint supernovae, with energy of 10^{51} erg, together with fallback and mixing (Umeda & Nomoto 2003). An alternative explanation is a double source with the lighter elements such as CNO, synthesised by faint SNe and the heavier elements by more conventional core-collapse SNe (Bonifacio et al. 2015). Spite et al. (2013) noted that the carbon abundance does not follow the iron decrease, but remains rather constant at the lowest metallicity. They suggested the existence of two groupsⁱⁱ: the former with high carbon abundance ($[\text{C}/\text{H}] \approx -2.0$), and a latter with lower carbon abundance ($[\text{C}/\text{H}] \approx -3.5$). The for-

[★] Based on ESPRESSO Guaranteed Time Observations collected at the European Southern Observatory under ESO programmes 1102.C-0744, 0103.D-0700, 0104.D-0688, 1104.C-0350, 108.2268.001, P.I. P. Molaro.

^{★★} E-mail: david.aguado@unifi.it

ⁱ Following Beers & Christlieb (2005) we will refer in this work with ultra metal-poor (UMP), hyper metal-poor (HMP), and mega metal-poor (MMP) to stars with $[\text{Fe}/\text{H}] < -4.0$, -5.0 , and -6.0 , respectively.

ⁱⁱ Some other authors split the CEMP-*no* into two groups depending on $[\text{Fe}/\text{H}]$ and $[\text{C}/\text{Fe}]$ (see Yoon et al. 2016, 2019 for more details).

mer group also shows enhancement of n-capture elements with $[\text{Ba}/\text{Fe}] > 1$, which is absent in the latter group. A different origin for carbon has been suggested in the two groups. In the *High-C* group, both carbon and the n-capture elements come from an asymptotic giant branch (AGB) companion, while the origin of carbon in the *Low-C* band is less certain, but should be pristine and should be coming from the SNe that polluted the gas from which the star is formed. This scenario implies that the *High-C* group consists of binaries while the *Low-C* group could be single or binary stars, but without a companion which experienced an AGB phase. This hypothesis has been tested with radial velocity studies in a small sample of metal-poor stars belonging to the two groups (Hansen et al. 2016a,b). Additional CEMP stars with $[\text{Fe}/\text{H}] < -4.5$ have been recently discovered revealing that all the CEMP stars with $[\text{Fe}/\text{H}] < -4.5$ belong to the CEMP-*no* group (Bonifacio et al. 2018b; Aguado et al. 2018b; Nordlander et al. 2019; González Hernández et al. 2020), and therefore are the preferred formation channel for the first low mass star formation.

HE 0107–5240 was employed by several groups to constrain the mass of the very first stars (see e.g. Bonifacio et al. 2003; Schneider et al. 2003; Umeda & Nomoto 2003). The existence of stars like HE 0107–5240 shows that stars with masses of the order of the sun or smaller do form at the lowest metallicities. Bromm & Loeb (2003) argued that the significant values of carbon and oxygen could have cooled the gas to permit low-mass star formation. However, the discovery of carbon normal stars such as SDSS J1029+1729 (Caffau et al. 2011a) and of Pristine 221.8781+9.7844 (Starkenbug et al. 2018) shows that not all the extremely metal-poor stars are carbon enhanced. More complex mechanisms for gas cooling such as dust cooling or turbulent fragmentation are required (Schneider et al. 2012; Greif et al. 2012).

The chemical study of HE 0107–5240 is remarkably challenging. Due to the extreme low metallicity, only nine elemental abundances (C, N, O, Na, Mg, Ca, Ti, Fe, and Ni) have been measured so far (Christlieb et al. 2002a, 2004; Collet et al. 2006). Significant upper limits were only possible for two n-capture elements, $[\text{Sr}/\text{Fe}] < -0.52$ and $[\text{Ba}/\text{Fe}] < 0.82$ (Christlieb et al. 2004). Understanding its kinematics was not simpler: more than 15 years after the discovery of HE 0107–5240, the first indication of binarity was found by Arentsen et al. (2019), which opened the possibility of a mass transfer from an AGB companion. This unexpected binarity behaviour was later confirmed by Bonifacio et al. (2020). Historically, it is interesting to note that the prototype of the CEMP-*no* star CS 22957–027, discovered almost simultaneously by Norris et al. 1997; Bonifacio et al. 1998, has also been shown to be a binary star with a period of about $P = 3125$ d by Preston & Sneden (2001).

In this work, we continue the radial velocities measurements with the aim to detail the binary properties of this ancient star. At the same time, we monitor the radial velocities, v_{rad} , for other CEMP-*no* stars with $[\text{Fe}/\text{H}] < -4.5$ to assess the fraction of binaries in this group.

2. ESPRESSO Observations and Data Reduction

The Echelle Spectrograph for Rocky Exoplanets and Stable Spectroscopic Observations (ESPRESSO), is a stable fibre-fed *échelle* spectrograph mounted at the incoherent focus of the Very Large Telescope (VLT) at Paranal Observatory, Chile, designed to measure velocities with precision as high as 10 cm s^{-1} (ESPRESSO, Pepe et al. 2021). In 2018 we started an ESO–GTO program, P.I. P. Molaro, to monitor radial velocities

Table 1: Targets observed in our ESPRESSO GTO program.

STAR	<i>Gaia</i> G mag	T_{eff} K	log g cgs	[Fe/H]	[C/Fe]	RUWE ^a
HE 0107–5240 ¹	14.9	5100	2.2	–5.39	4.00	1.01
SDSS J0023+0307 ^{2,3}	17.6	6140	4.8	< –5.50	>3.31	0.95
HE 0233–0343 ⁴	15.3	6100	3.4	–4.68	3.32	1.02
SMSS 0313–6708 ⁵	14.5	5125	2.3	< –7.10	>5.39	1.02
HE 0557–4840 ⁶	15.2	4900	2.2	–4.75	1.66	1.07
SDSS J1313–0019 ^{7,8}	15.2	5170	2.6	–5.00	3.00	0.99
HE 1327–2326 ⁹	13.4	6180	3.7	–5.60	4.26	0.98
SMSS 1605–1443 ¹⁰	15.4	4850	2.0	–6.21	3.89	1.06

^aThe Renormalised Unit Weight Error could be used to detect variability (see text).

Notes. (1) Christlieb et al. (2002b); (2) Aguado et al. (2018a); (3) Aguado et al. (2019); (4) Hansen et al. (2014); (5) Keller et al. (2014); (6) Norris et al. (2007); (7) Allende Prieto et al. (2015); (8) Frebel et al. (2015); (9) Frebel et al. (2005); (10) Nordlander et al. (2019).

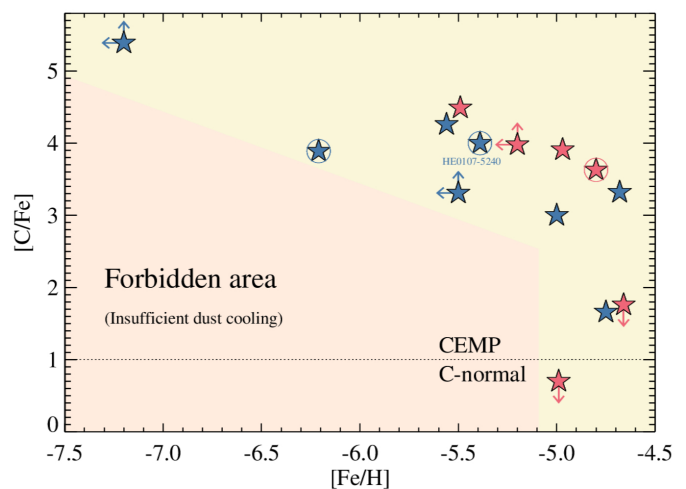


Fig. 1: $[\text{C}/\text{Fe}]$ – $[\text{Fe}/\text{H}]$ plane for all the stars observed with ESPRESSO (blue symbols), and for other metal-poor stars (red symbols). Stars with confirmed (HE 0107–5240 and SDSS J0929+0238) and indicated (SMSS 16054–1443) binarity are marked with a circle. According to Chiaki et al. (2017), the region where no low-mass star formation is permitted is also red-filled.

of the most metal-poor stars to probe their binarity. The spectrograph has two fibers with a core diameter of $140 \mu\text{m}$ corresponding to a $1''.0$ aperture in the sky. While Fibre A was centered onto the object, Fibre B was in the sky. The binning of the CCD was initially 2×1 pixel and, when it became available, 4×2 , always with a slow readout mode. Observations were done in single UT configuration mode with exposure times between $t_{exp} = 1800$ and $t_{exp} = 3600$ s, the maximum allowed by service mode operation. A total of 50 h (time on target) have been observed during this -still ongoing- program. The observing conditions were restricted as follows: airmass ≤ 1.5 , seeing $\leq 1''.0$, water vapour ≤ 30 mm and minimum lunar distance = 30° . Data reduction was performed by the automatic ESPRESSO pipeline including sky subtraction, bias and flat-fielding correction. The wavelength calibration is the one which combines the ThAr lamp with a Fabry–Pérot Etalon (Pepe et al. 2013). The signal-to-noise ratio of individual exposures close to the G-band ($\lambda \sim 4300 \text{ \AA}$) spanned the range $5 \leq \text{SNR} \leq 20$, depending on the observing time and the magnitude of the target. We retrieved an additional exposure taken with HARPS at the ESO 3.6 m telescope

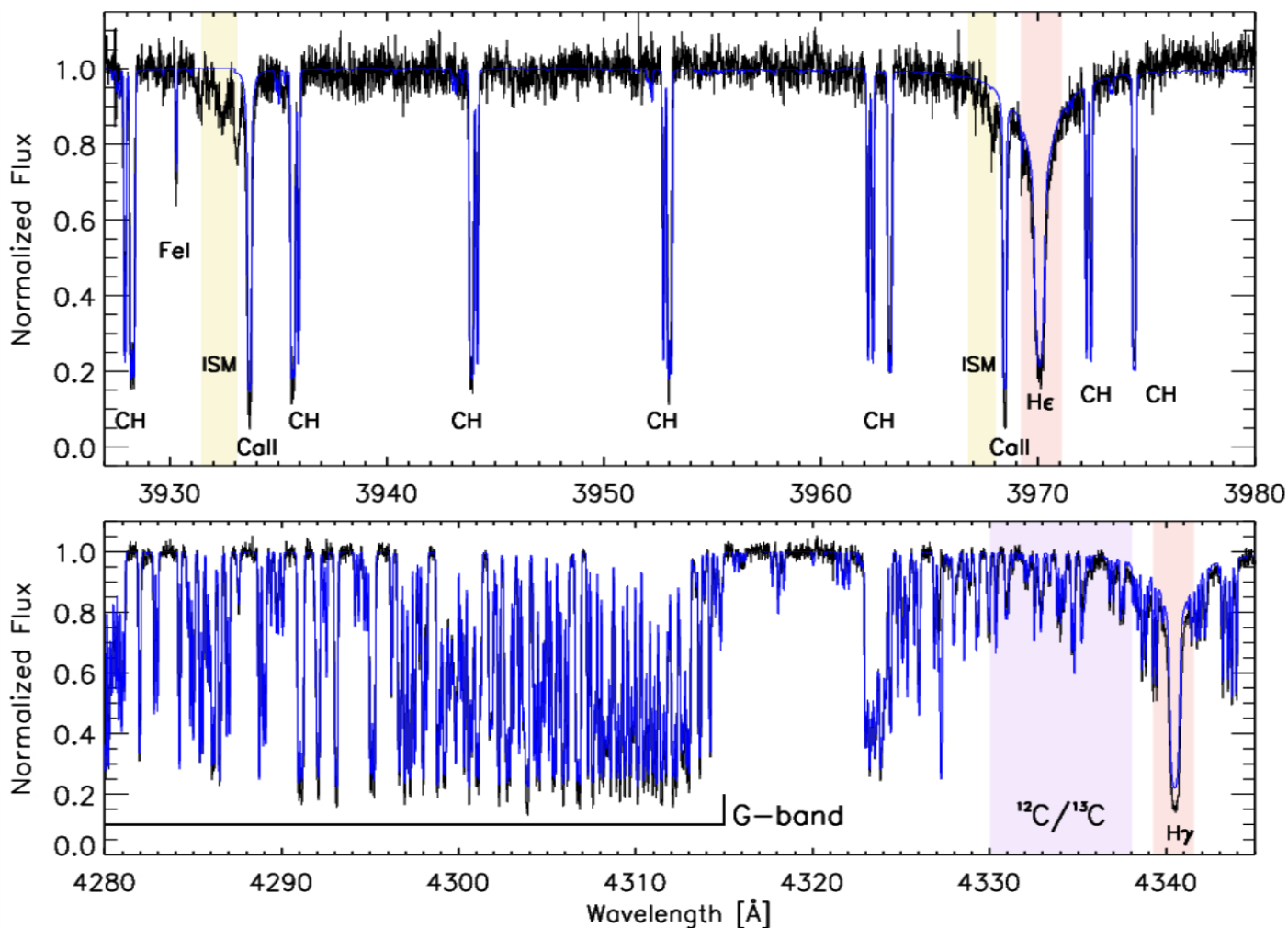


Fig. 2: A narrow region of the co-added ESPRESSO spectrum of HE 0107–5240 (black lines), around the Ca H&K area (upper panel) and the G-band (lower panel) together with a SYNTH model computed to match the HE 0107–5240 stellar parameters (blue line). Absorptions corresponding to the Balmer series and interstellar Ca II are marked in red and yellow respectively. The region from which we measure the $^{12}\text{C}/^{13}\text{C}$ ratio is marked in viola. Other metallic absorptions and the G-band, are also labelled.

of HE 0107–5240. The observation was made in Technical Time in the high-resolution mode “HAM”. Observing time was 3600 s and SNR ~ 2 at 4300 Å with a seeing of 0.75”.

While our primary target is HE 0107–5240, with 17 visits, the program also included ESPRESSO observations for seven more CEMP-*no* stars with $[\text{Fe}/\text{H}] < -4.5$. In table 1 all the observed targets and their main stellar parameters are summarised. The situation of these primitive stars in the $[\text{C}/\text{Fe}]-[\text{Fe}/\text{H}]$ plane is shown in Fig. 1, together with other metal-poor stars that are not included in our program for various reasons that will be discussed in Section 8.

3. Radial Velocity Determination

The ESPRESSO radial velocity precision allows us to detect binary systems even if they show long periods (up to several decades) and relatively small radial velocity changes in a period of time of a few years.

The measurements of the stellar radial velocities are performed in two steps.

- First, a synthetic model with the SYNTH code (Kurucz 2005; Sbordone 2005) is computed by assuming stellar parameters and abundances from the literature values (Christlieb et al. 2004). Then we smoothed and resampled the synthetic spectra to the ESPRESSO (and HARPS) resolving power of $R \sim 140,000$ (and $R \sim 115,000$) and to the same lambda step. Subsequently, we normalised the observed spectra and interpolated both data and the template to the same wavelength. A cross-correlation function (CCF) was performed in the Fourier Space by using the algorithm by Tonry & Davis (1979) which contained the `noao.rv` package within IRAFⁱⁱⁱ (Tody 1993) environment over the 4200–4315 Å interval, where the CH absorptions are detectable in individual exposures.
- Second, we corrected each exposure by the shift derived from the CCF and combined all the spectra in the rest of frame with a 3σ -clip algorithm to compute a high SNR “natural” template. An example of this coadded spectrum of

ⁱⁱⁱ IRAF is distributed by the National Optical Astronomy Observatory which is operated by the Association of Universities for Research in Astronomy (AURA) under a cooperative agreement with the National Science Foundation.

Table 2: Radial velocities measurements from ESPRESSO.

STAR	v_{rad} (km s ⁻¹)	error (km s ⁻¹)	MJD ^a -50000	MODE	t_{exp} s	CCF	Comment ^b
HE 0107-5240	48.049	0.034	8364.107	HR21	3300	CH (G-band)	
HE 0107-5240	48.083	0.104	8473.127	-	3600	CH (G-band)	HARPS
HE 0107-5240	47.833	0.010	8698.313	HR21	3400	CH (G-band)	
HE 0107-5240	47.771	0.010	8721.263	HR21	3400	CH (G-band)	
HE 0107-5240	47.786	0.009	8730.206	HR21	3400	CH (G-band)	
HE 0107-5240	47.818	0.012	8741.250	HR21	3400	CH (G-band)	
HE 0107-5240	47.846	0.012	8759.096	HR21	3400	CH (G-band)	
HE 0107-5240	47.697	0.012	9190.096	HR21	3417	CH (G-band)	
HE 0107-5240	47.625	0.012	9237.032	HR42	3417	CH (G-band)	
HE 0107-5240	47.562	0.018	9427.332	HR21	3600	CH (G-band)	
HE 0107-5240	47.533	0.012	9435.176	HR42	3600	CH (G-band)	
HE 0107-5240	47.542	0.010	9435.219	HR42	3600	CH (G-band)	
HE 0107-5240	47.508	0.013	9489.238	HR21	3000	CH (G-band)	
HE 0107-5240	47.505	0.009	9618.061	HR42	3310	CH (G-band)	
HE 0107-5240	47.497	0.011	9529.202	HR42	3200	CH (G-band)	
HE 0107-5240	47.509	0.008	9545.123	HR42	3200	CH (G-band)	
HE 0107-5240	47.436	0.013	9606.042	HR42	3600	CH (G-band)	
SDSS J0023+0307	-195.540	0.107	8761.245	HR21	3400	Mg I b	Synthetic template
SDSS J0023+0307	-195.035	0.171	8805.034	HR21	3400	Mg I b	Synthetic template
SDSS J0023+0307	-195.761	0.102	8835.044	HR21	3400	Mg I b	Synthetic template
HE 0233-0343	52.058	0.027	8699.288	HR21	3400	CH (G-band)	
HE 0233-0343	52.127	0.021	8760.318	HR21	3400	CH (G-band)	
HE 0233-0343	52.169	0.024	8783.112	HR21	3400	CH (G-band)	
HE 0233-0343	51.074	0.024	8813.243	HR21	3400	CH (G-band)	
SMSS 0313-6708	298.643	0.043	8701.281	HR21	3400	CH (G-band)	
SMSS 0313-6708	298.677	0.042	8732.245	HR21	3400	CH (G-band)	
SMSS 0313-6708	298.509	0.033	8732.343	HR21	3400	CH (G-band)	
SMSS 0313-6708	298.710	0.043	8740.153	HR21	3400	CH (G-band)	
SMSS 0313-6708	298.581	0.039	8740.196	HR21	3400	CH (G-band)	
SMSS 0313-6708	298.632	0.046	8742.119	HR21	3400	CH (G-band)	
SMSS 0313-6708	298.578	0.042	8743.268	HR21	3400	CH (G-band)	
SMSS 0313-6708	298.531	0.047	8743.335	HR21	3400	CH (G-band)	
SMSS 0313-6708	298.536	0.050	8780.153	HR21	3417	CH (G-band)	
SMSS 0313-6708	298.650	0.036	9190.052	HR42	3417	CH (G-band)	
SMSS 0313-6708	298.603	0.038	9237.078	HR42	3417	CH (G-band)	
SMSS 0313-6708	298.530	0.027	9250.041	HR42	3417	CH (G-band)	
SMSS 0313-6708	298.486	0.039	9264.017	HR42	3000	CH (G-band)	
HE 0557-4840	212.209	0.028	8761.333	HR21	3400	Mg I b	
HE 0557-4840	212.172	0.026	8762.327	HR21	3400	Mg I b	
HE 0557-4840	212.199	0.027	8834.084	HR21	3400	Mg I b	
HE 0557-4840	212.198	0.023	8864.083	HR21	3400	Mg I b	
SDSS J1313-0019	273.984	0.054	9649.249	HR42	3444	CH (G-band)	Synthetic template
HE 1327-2326	63.801	0.040	8615.137	HR21	1800	CH (G-band)	
HE 1327-2326	63.636	0.037	8688.022	HR21	2700	CH (G-band)	
HE 1327-2326	63.709	0.041	8688.055	HR21	2700	CH (G-band)	
HE 1327-2326	63.655	0.027	8695.996	HR21	1800	CH (G-band)	
HE 1327-2326	63.639	0.037	8697.988	HR21	2400	CH (G-band)	
HE 1327-2326	63.697	0.041	8841.331	HR21	1800	CH (G-band)	
HE 1327-2326	63.601	0.036	9429.054	HR42	3000	CH (G-band)	
HE 1327-2326	63.700	0.016	9663.072	HR42	2844	CH (G-band)	
SMSS 1605-1443	-226.059	0.037	9676.277	HR42	3150	CH (G-band)	
SMSS 1605-1443	-226.118	0.036	9726.189	HR42	3150	CH (G-band)	
SMSS 1605-1443	-226.196	0.037	9727.060	HR42	3150	CH (G-band)	
SMSS 1605-1443	-226.214	0.030	9761.059	HR42	3150	CH (G-band)	
SMSS 1605-1443	-226.278	0.033	9792.055	HR42	3150	CH (G-band)	

Notes. ^(a) Modified Julian date at the start of observation. ^(b) Measurements obtained from a synthetic template are indicated (See text for details).

HE 0107–5240 is shown in Fig. 2. Similarly to the previous step, we normalised the combined spectrum and calculated a new CCF for each individual exposure obtaining our final v_{rad} values.

The radial velocities given by the CCF are summarised in Table 2. Focusing in HE 0107–5240, the average error we have from ESPRESSO data is 13 m s^{-1} , 8 times lower than the one from HARPS, 104 m s^{-1} . We also notice the radial velocity of the #1 ESPRESSO observation taken on 3rd September 2018 is in common with Bonifacio et al. (2020) and the two measurements are consistent at 1.5σ . This small difference is mostly attributed to the fact that the CCF of Bonifacio et al. (2020) is performed over a different range, $4000\text{--}4498 \text{ \AA}$, including other lines which show some velocity offset with respect to the CH molecular absorption. In the next section we present a complete kinematical analysis based in the results we obtained for HE 0107–5240 from ESPRESSO data and from other sources in the literature.

4. Binarity of HE 0107–5240

The radial velocities of HE 0107–5240 show a monotonically decreasing trend and therefore we confirm that this is a binary star with a long period. The overall rate of change in this period is of $\sim 0.5 \text{ m s}^{-1} \text{ d}^{-1}$, which is consistent with previous results by Arentsen et al. (2019); Bonifacio et al. (2020).

To constrain the kinematical properties of the binary star HE 0107–5240 together with the ones derived in this work we take advantage of previous v_{rad} measurements from Christlieb et al. (2004, UVES at VLT), Arentsen et al. (2019, HRS at SALT) and Bonifacio et al. (2020, ESPRESSO at VLT). The v_{rad} data are binned in 1-d bins to limit the stellar jitter. This only affects the UVES data reducing the number of points from 33 to 17 (See Fig. 3, upper-left panel). The HRS points with v_{rad} errors larger than 2.0 km s^{-1} have been discarded from Fig. 3 (upper-middle panel). All the RVs are modelled using the RADVEL (Fulton et al. 2018)^{iv} including a Keplerian motion of the star plus an RV offset (the γ of the v_{rad} curve), and a jitter parameter for each instrument within a likelihood scheme implemented in python using CELERITE (Foreman-Mackey et al. 2017)^v. Unfortunately, there are no contemporaneous observations of different instruments, except for the single HARPS RV point, that would allow us to derive any possible RV offset between different instruments, but the jitter may be absorbing part of this possible offset with an uncertainty which propagates onto the uncertainties on orbital period, semi-amplitude velocity and eccentricity. The Keplerian orbit is described as:

$$v_{rad} = \gamma + k_2(\cos(v_a + \omega) + e \cos(\omega)) \quad (1)$$

where the true anomaly v_a is related to the solution of the Kepler equation that depends on the orbital period, P_2 , the orbital semi-amplitude velocity, k_2 , the argument of periastron, ω , and the eccentricity of the orbit, e . The RADVEL allows to infer both the time of periastron, $T_{2,peri}$, and the time at inferior conjunction of the star, $T_{2,conj}$. Following Fulton et al. (2018), we chose to perform fitting and posterior sampling using the $\ln P_2$, $T_{2,conj}$, $\sqrt{e} \cos \omega$, $\sqrt{e} \sin \omega$, $\ln k_2$ basis which helps to speed the convergence. We chose $\ln k_2$ to avoid favouring large k_2 and $\ln P_2$ because P_2 may

^{iv} RADVEL is a Python package for modeling of radial velocity time series data, available in <https://radvel.readthedocs.io/en/latest/index.html>

^v CELERITE is a library for fast and scalable Gaussian Process (GP) Regression in one dimension, available in <https://celerite.readthedocs.io/en/stable/>

Table 3: Orbit parameters of HE 0107–5240 from the MCMC analysis.

Parameter	MCMC Priors	Results
Keplerian orbit		
k_2 [km s^{-1}]	$\mathcal{LU}(0.1, 5)$	$1.78^{+0.16}_{-0.11}$
P_2 [d]	$\mathcal{LU}(1000, 75000)$	13009^{+1496}_{-1370}
$T_2 - 2450000$ [d]	$\mathcal{U}(-4000, 3500)$	-1630^{+1246}_{-1438}
ω [rad]	$\mathcal{U}(-\pi, \pi)$	$-1.81^{+0.27}_{-0.41}$
e	$\mathcal{U}(0, 1)$	$0.31^{+0.11}_{-0.10}$
Other terms		
jitter _{UVES} [km s^{-1}]	$\mathcal{LU}(0.01, 5.0)$	$0.21^{+0.06}_{-0.05}$
jitter _{HRS} [km s^{-1}]	$\mathcal{LU}(0.01, 5.0)$	$0.09^{+0.29}_{-0.07}$
jitter _{ESPRESSO} [km s^{-1}]	$\mathcal{LU}(0.01, 5.0)$	$0.03^{+0.01}_{-0.01}$
jitter _{HARPS} [km s^{-1}]	$\mathcal{LU}(0.01, 5.0)$	$0.09^{+0.24}_{-0.07}$
$\gamma - 46.5$ [km s^{-1}]	$\mathcal{U}(-3.0, 3.0)$	$0.27^{+0.14}_{-0.19}$

be long if compared with the observational baseline. The v_{rad} errors in the Fig. 3 include the jitter of each instrument and the v_{rad} offset has been subtracted. In addition, we adopted uniform priors for all parameters (see Table 3).

To sample the posterior distributions and obtain the Bayesian evidence of the model (that is, marginal likelihood, $\ln Z$), we relied on nested sampling using DYNESTY (Speagle 2020)^{vi}. We initialized a number of live points equal to $N^3(N + 1)$, to efficiently sample the parameter space, with $N = 10$ being the number of free parameters. The resulting posterior distributions are displayed in Fig. 4 together with the orbital parameters of the star. In the middle panel of Fig. 3 we also show in grey a subsample of 300 models randomly selected from the final selection of $\sim 37,696$ Bayesian samples from the posterior distributions displayed in Fig. 4. On the other hand, the binary mass function can be computed from the masses of the binary component (e.g. Tauris & van den Heuvel 2006), i.e. that of the seen star, M_2 , and that of the unseen binary companion, M_1 , and the orbital parameters as follows:

$$f(M) = (M_1^3 \sin^3 i) / (M_1 + M_2)^2 \quad (2)$$

$$f(M) = [(P_{orb} k_2^3) / (2\pi G)] (1 - e^2)^{3/2} \quad (3)$$

With the Bayesian samples we computed the posterior distribution of the binary mass function providing the following result:

$$f(M) = 0.007^{+0.002}_{-0.001} [M_\odot] = 7.0^{+1.7}_{-1.4} [M_{Jup}] \quad (4)$$

Depending on the ratio of masses between the seen and unseen objects of the binary, usually the binary mass function provides a lower limit to the mass of the unseen companion. In general, the minimum mass of this companion can be approximately estimated as the maximum value between f and $f^{1/3} M_2^{2/3}$, thus giving $M_1 [M_\odot] > 0.16$, when adopting a mass of $M_2 [M_\odot] = 0.8$ for the seen star HE 0107–5240.

The minimum orbital distance (or semi-major axis) of the star with respect to the center of mass of the binary system can be computed as :

$$a_2 \sin i = [(P_{orb} k_2) / (2\pi)] (1 - e^2)^{1/2} \quad (5)$$

^{vi} DYNESTY is a Pure Python, MIT-licensed Dynamic Nested Sampling package for estimating Bayesian posteriors and evidences, available in <https://dynesty.readthedocs.io/en/stable/>

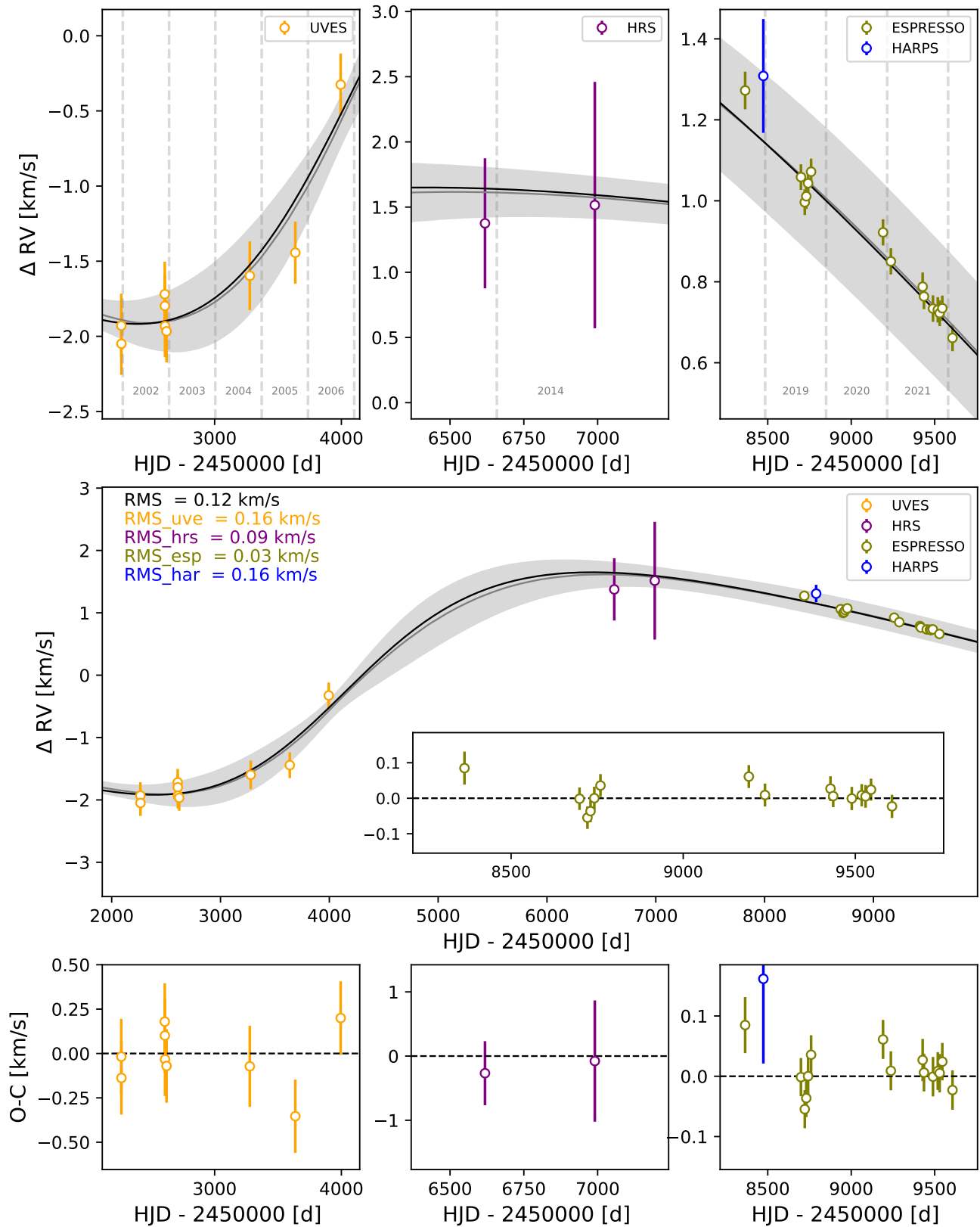


Fig. 3: Radial velocity (RV) points of HE 0107–5240 versus heliocentric Julian date (HJD), together with the best RV model. The inner panel within the middle panel shows the ESPRESSO RV points only after removing the best RV model. Within the middle panel we provide the RMS of the residuals of all RVs and those from each spectrograph given in the bottom panels.

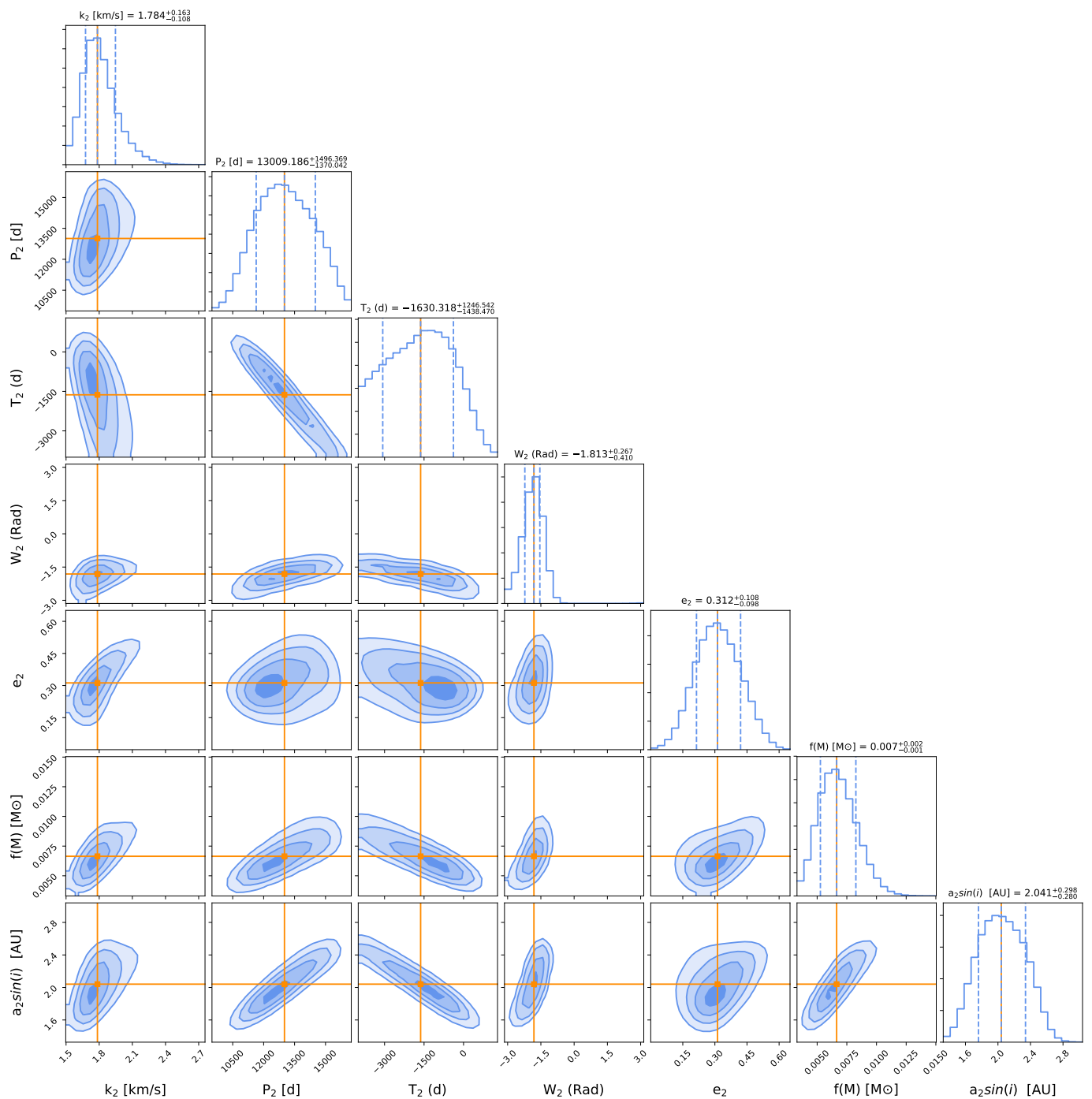


Fig. 4: Posterior distributions of the star’s orbital parameters of the RV model and two additional parameters, the binary mass function, $f(M)$, and the star’s orbital distance to the center of mass, $a_2 \sin i$, inferred from the orbital parameters.

The orbital period of the binary is 35.6 ± 4.1 yr. Using the Bayesian samples we also calculated the posterior distribution of the minimum orbital distance (or semi-major axis of the star’s orbit) at $a_2 \sin i = 2.04 \pm 0.30$ AU (see Fig. 4). We note, as a comparison, Jupiter’s orbit in the solar system shows a semi-major axis of about 5.2 AU and an orbital period of 11.9 yr.

5. A hint for a secondary motion?

The dispersion of the ESPRESSO radial velocities after subtracting the best fit is 35 m s^{-1} , which is in line with the derived velocity jitter (Table 3). However, this is about 3 times greater than the mean error bar of the ESPRESSO radial velocity measurements, suggesting the presence of additional signal of relatively smaller amplitude. Careful inspection of the ESPRESSO velocity residuals (see bottom panel of Fig. 3) indicates variability time scales of the order of tens to hundreds of

days. We analyzed the residuals after the fit using the Generalized Lomb Scargle periodogram (GLS, Zechmeister & Kürster 2009). The GLS is an algorithm for detecting periodicities in unevenly sampled time-series, equivalent to least-squares fitting of sine waves, that generalizes the Lomb-Scargle periodogram (Scargle 1982) by including a floating zero-point and weights to the individual datapoints. We computed the GLS between 2 and 1000 d and found no significant peak with a false-alarm probability smaller than 10%. This is not surprising given the small number of ESPRESSO data.

One possible scenario to account for the variability of the ESPRESSO velocity residuals is the existence of pulsations in HE 0107–5240. However, oscillations have their characteristic frequency at shorter time scales. Theory predicts that the longest period for first overtone pulsators increases as the metal content decreases, being of about 9 days at $Z = 0.0004$ and of about 6 days at $Z = 0.004$ (Marconi et al. 2010). Creevey et al. (2019) reported the first detection of sun-like oscillations in the moderately metal poor giant star HD 122563 ($\text{Fe}/\text{H} = -2.80 \pm 0.15$) (Jofré et al. 2014) using hundreds of radial velocity measurements obtained with a mean cadence of one observation per day. They found a characteristic frequency at $3.07 \pm 0.05 \mu\text{Hz}$ (3.77 ± 0.06 d) for the oscillations. Interestingly, they also found an additional signal in the form of a long-term trend with a velocity amplitude and time scale similar to those of HE 0107–5240. In HD 122563, the velocity amplitude and period of the trend are about 120 m s^{-1} and 300 d, respectively. Creevey et al. (2019) favored stellar accretion, activity, and rotation against oscillations to explain the trend because the time scale of the long-term variation is far from the expected intrinsic pulsation periods.

A second scenario is stellar activity that may produce variations in the ESPRESSO radial velocities modulated by the rotation of the star. Ceillier et al. (2017) found that $\approx 2\%$ of the giant stars are actually fast rotators with rotation periods of less than 170 d. Adopting the mass of $0.8 \pm 0.1 M_{\odot}$ and the surface gravity of $\log g[\text{cm s}^{-2}] = 2.2 \pm 0.1$ (Christlieb et al. 2004), the estimated stellar radius of HE 0107–5240 is determined at $11.8_{-2.0}^{+2.2} R_{\odot}$, which combined with periods of 50–200 d (time-scale of the radial velocity variability) would yield equatorial rotational velocities of $2\text{--}13 \text{ km s}^{-1}$ when the star is seen equator-on. This rotational velocity is measurable with high-resolution spectrographs like ESPRESSO, but we do not detect any significant rotational broadening in the spectra ($v \sin i \leq 2 \text{ km s}^{-1}$). This implies that either HE 0107–5240’s rotation axis is likely inclined, or periods of ten to a few hundred days are too short for them to be ascribed to the star’s rotation. The Transiting Exoplanet Survey Satellite (*TESS*, Ricker et al. 2015) observed HE 0107–5240 in sectors 2 (2018 Aug 23 – 2018 Sep 19) and 29 (2020 Aug 26 – 2020 Sep 21). The exposure times were 1426 s for the former and 475 s for the latter sector. Each *TESS* sector covers about 25 d (slightly shorter than the time scales of the spectroscopic variability) and the two sectors were observed two years apart. We downloaded the target pixel file products from the Mikulski Archive for Space Telescopes and processed them with the *lightkurve* software (Barentsen et al. 2021). We found rather flat light curves with no obvious photometric variability higher than $\sim 5\%$ (confidence of 3σ). We conclude that with the data in hand, the stellar activity scenario cannot be discarded.

A third scenario is the presence of giant planets around HE 0107–5240 with orbital periods of less than a few hundred days, which are the ones capable of imposing velocity amplitudes of the order of several tens m s^{-1} on their parent star. We explored this hypothesis by fitting one and two Keplerian models with null eccentricity to the ESPRESSO velocity residuals

finding that the two-planet model with velocity amplitudes of ≈ 30 and 40 m s^{-1} is preferred by the Bayesian statistics. The two planets would have minimum masses of ≈ 0.5 and $1.0 M_{\text{Jup}}$ and orbital periods below 200 d. However, there is neither a sufficient number of radial velocity measurements nor there is the cadence of the spectroscopic data adequate for an in-depth planetary analysis. Studying further this scenario is beyond the scope of this paper.

We remark, however, that should the presence of giant planets orbiting the hyper metal-poor star HE 0107–5240 be confirmed, this would challenge the core accretion theory of planet formation because heavy elements are needed to cool down the gas of the protoplanetary disk and form the dust grains that settle into the midplane and coagulate to create the planetesimals (Johnson & Li 2012).

A fourth scenario is actually the mixture of two or more scenarios above. More ESPRESSO data are planned to rule out any hypotheses.

6. Improved Chemistry of HE 0107–5240

The high quality of the combined spectrum shown in Fig. 2 allow us to perform detailed chemical analysis beyond that existing works about HE 0107–5240 in the literature. The stellar parameters of this star are of $T_{\text{eff}} = 5200 \text{ K}$, $\log g = 2.2$ and microturbulence of $v_{\text{mic}} = 2.2 \text{ km s}^{-1}$ are taken from Christlieb et al. (2004). We computed different stellar models by using the SYNTHE code (Kurucz 2005; Sbordone 2005) along with the ATLAS9 model atmosphere code. In table 4 we measured 21 Fe I lines from ESPRESSO data (See Table 4) leading to a $A(\text{Fe I}) = 1.96 \pm 0.13$. By assuming $A(\text{Fe I})_{\odot} = 7.52$ (Caffau et al. 2011b; Lodders 2019), we end up with $[\text{Fe}/\text{H}] = -5.56 \pm 0.13$ while the preferred metallicity originally reported by Christlieb et al. (2004) was $[\text{Fe}/\text{H}]_{\text{LTE}} = -5.39 \pm 0.20$. In Table 4 the lines and the derived abundances are reported and compared with those of Christlieb et al. (2004). The general abundances are confirmed and some more lines are observed. In general, the derived abundances are slightly lower than those originally derived. Few significant improvements are obtained. The measured $^{12}\text{C}/^{13}\text{C}$ ratio implies that the star is unmixed (i.e., chemically unmixed, Spite et al. 2006, Fig. 3c). The previous upper limits were $[\text{Sr}/\text{Fe}] \leq -0.52$ and $[\text{Ba}/\text{Fe}] \leq +0.82$ Christlieb et al. (2004) are now improved into $[\text{Sr}/\text{Fe}] \leq -0.76$ and $[\text{Ba}/\text{Fe}] \leq +0.20$. In particular, the latter now allows to classify HE 0107–5240 as a CEMP-*no* with confidence, which requires $[\text{Ba}/\text{Fe}] < 1.0$. The upper limit on the lithium is now determined at $A(\text{Li}) < 0.5$. In Fig. 5, we show our new $^{12}\text{C}/^{13}\text{C}$ measurement and the more constraining upper limits on Li, Sr, and Ba.

7. Speckle observations of HE 0107–5240

HE 0107–5240 is a binary system but the mass and nature of the companion are uncertain. A giant is excluded since it would outshine any unevolved companion (Bonifacio et al. 2020). Arntsen et al. (2019) suggested that the companion is a white dwarf which in its AGB phase transferred mass to the currently observed giant. Unfortunately, the spectral energy distribution (SED) of HE 0107–5240 does not provide useful indications for the companion star. HE 0107–5240 is detected in *NUV* filter ($\lambda_{\text{eff}} = 213.6 \text{ nm}$) but not in the *FUV* filter ($\lambda_{\text{eff}} = 153.9 \text{ nm}$) of GALEX survey (Bianchi et al. 2011). Venn et al. (2014) explored the spectral energy distribution from 444 nm to 22080 nm claiming a marginal detection of an IR excess in the WISE W3 band ($\lambda_{\text{eff}} = 11560 \text{ nm}$).

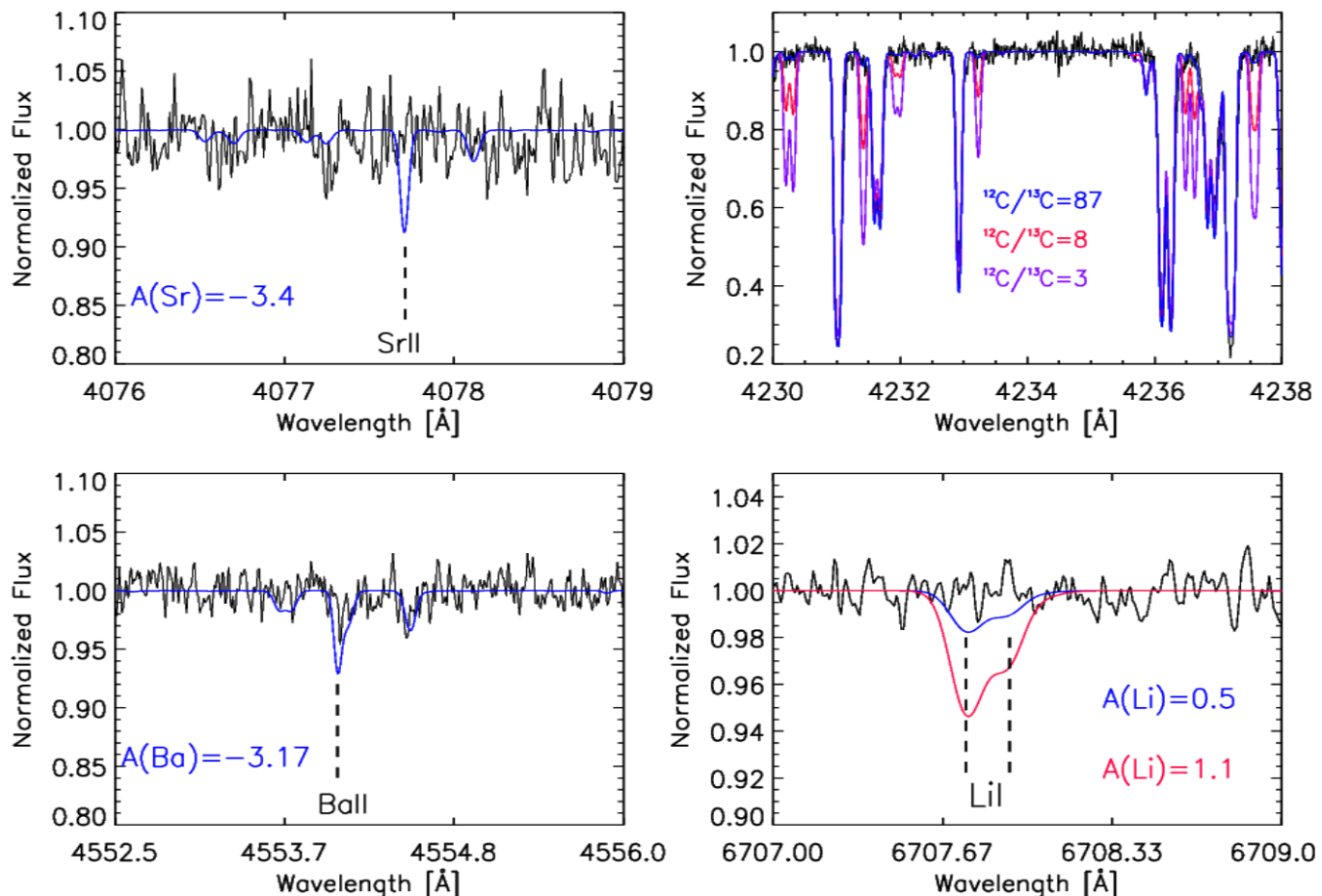


Fig. 5: A narrow region of the ESPRESSO combined spectrum of HE 0107–5240 around the Sr II line at 4077.7 Å (upper-left), the G-band (upper-right), the Sr II line at 4554.0 Å (lower-left), and the Li doublet at 6707.8 Å (lower-right). Derived values and adopted upper limits are shown in blue. Remarkably, at the ESPRESSO resolution the asymmetry in the profile of Li doublet is clear and the upper limit ($A(\text{Li}) < 0.5$) is much more constraining than the UVES value from Christlieb et al. (2004) ($A(\text{Li}) < 1.1$) in red.

In order to set further limits on the nature of the companion star, we exploit speckle imaging on the Gemini 8-m telescope which provides an angular resolution equal to the diffraction limit of the telescope and fairly deep image contrast levels. We observed HE 0107–5240 on 2019 September 16 UT and 2019 October 8 UT using the Zorro speckle instrument mounted on the 8 m Gemini-South telescope located on Cerro Pachon, Chile (Scott et al. 2021; Howell & Furlan 2022). Zorro uses a dichroic to split the optical light at 674 nm and obtains simultaneous blue and red images onto two Andor EMCCD detectors. Both observations of HE 0107–5240 gave consistent results, but the October observations occurred under better seeing, thus the image contrast achieved was slightly larger. The 8 Oct 2021 UT observation consisted of a total on-source time of 15 minutes bracketed by observations of point-spread function (PSF) standard stars HR 0242 and HR 0667. The observation collected 1200 images of 60 ms which are then subjected to Fourier analysis techniques and used to search for close companions, to determine their properties, and provide reconstructed high resolution images (see Howell et al. 2011).

Figure 6 shows the achieved image contrast curves (differential magnitude as a function of the projected angular separation to the central star) for the Oct 2019 HE 0107–5240 observation. The angular limits extend from the 8-m diffraction limit,

near 20 mas, out to the speckle correlation limit near 1.2 arcsec. No companion star was detected with differential magnitudes of less than 4 mag (562 nm) and 5.8 mag (832 nm) around HE 0107–5240. Any fainter source would have not been seen by the Speckle observations. This is not surprising giving the distance to HE 0107–5240 of ≈ 11 Kpc, as the angular limits of 20 mas to 1.2 arcsec correspond to a linear distance of about 220 AU to 13,200 AU from the primary. The inner working angle distance is not far away from the approximate distance of a secondary clump (≈ 150 AU) in the simulations of protostar formation from clouds with primordial chemistry of Becerra et al. (2015) but much higher than the few AU of the kinematical motion described in Sec 4.

8. Follow-up of CEMP-*no* stars with $[\text{Fe}/\text{H}] < -4.5$

At the time of writing there are 12 CEMP-*no* stars and 2 Carbon-normal stars with $[\text{Fe}/\text{H}] < -4.5$. As part of the same GTO ESPRESSO program, besides HE 0107–5240, we targeted 7 more relatively bright CEMP-*no* stars living in the most metal-poor regime. The remaining 6 objects already identified as primitive stars with $[\text{Fe}/\text{H}] < -4.5$ have not been observed in this program for various reasons. For the sake of completeness we briefly comment on them:

Table 4: Abundances of HE 0107–5243 from the ESPRESSO spectrum. In the 6th column the abundances from Christlieb et al. (2004) are given for comparison. In the column for comments some possible blends are indicated.

Specie	Ion	$\lambda(\text{\AA})$	$A(X)_{\odot}^{(1)}$	$A(X)$	$A(X)_{\text{Ch04}}$	R.I.	$[X/\text{Fe}]^2$	Notes
Li		3.00	6707.76	1.04	<0.50	<1.1	–	
C		6.00	G-band	8.58	6.90	6.81	–	+3.88
$^{12}\text{C}/^{13}\text{C}$		6.00	G-band	91.4	87	~60	–	–
N		7.00	CN	8.00	5.00	5.22	–	+2.56
Na		11.00	5889.951	6.28	1.62	1.83	–	+0.90
Na		11.00	5895.924		1.62	1.90	–	+0.90
Mg		12.00	3829.355	7.50	2.15	–	0.47	+0.21
		12.00	3832.304		2.22	–	0.34	+0.29
		12.00	3838.292		2.09	–	0.23	+0.15
		12.00	5167.321		2.33	–	0.88	+0.39
		12.00	5172.684		2.31	2.38	0.65	+0.37
		12.00	5183.604		2.31	2.45	0.53	+0.37
Al		13.00	3961.520	6.41	<0.90	<0.93	0.58	<+0.05
K		19.00	7698.964	5.10	<1.22	–	–	+1.68
Ca		20.01	3933.663	6.34	1.39	1.44	0.15	+0.61
		20.01	3968.469		1.47	–	0.15	+0.69
		20.00	4226.728		0.78	0.99	0.63	+0.00
Cr		24.00	5204.511	5.62	<1.07	–	0.99	+1.01
		24.00	5206.023		<0.87	–	–	+0.81
		24.00	5208.425		<0.67	–	0.97	+0.61
Fe		26.00	3820.425	7.52	1.71	1.91	0.23	-0.25
		26.00	3824.444		2.01	2.30	0.49	+0.05
		26.00	3825.881		1.73	1.99	0.32	-0.23
		26.00	3827.822		1.93	–	0.70	-0.03
		26.00	3834.222		1.85	–	0.51	-0.11
		26.00	3859.911		1.79	2.08	0.19	-0.17
		26.00	3878.573		2.04	–	0.57	+0.08
		26.00	3886.282		1.98	–	0.36	+0.20
		26.00	3899.707		2.13	–	0.66	+0.19
		26.00	3922.912		2.18	2.24	0.71	+0.22
		26.00	3930.297		2.11	–	0.70	+0.15
		26.00	4045.812		1.90	2.03	0.52	-0.06
		26.00	4063.594		1.92	2.00	0.69	-0.04
		26.00	4071.738		1.97	2.17	0.76	+0.01
		26.00	4143.868		1.95	–	0.89	-0.01
		26.00	4202.029		2.14	–	0.92	+0.18
		26.00	4250.787		1.88	–	0.94	-0.08
		26.00	4325.762		1.91	–	0.76	-0.05
		26.00	4383.545		1.93	–	0.58	-0.04
		26.00	5269.537		2.08	2.20	0.91	+0.12
		26.00	5328.039		2.08	–	0.94	+0.12
Sr		38.01	4077.709	2.92	<-3.40	<-2.83	0.48	<-0.76
		38.01	4215.519		<-3.40	<-2.53	0.65	<-0.76
Ba		56.01	4554.029	2.19	<-3.17	–	0.91	<+0.20
		56.01	4934.076		<-2.87	<-2.33	0.95	<+0.50

Notes. ⁽¹⁾ Solar abundances from Lodders (2019)

⁽²⁾ Chemical ratios, $[X/\text{Fe}]$, are based in our derived LTE metallicity: $[\text{Fe}/\text{H}] = -5.56 \pm 0.13$

- SDSS J1035+0641 ($G_{\text{mag}} = 18.4$, $[\text{Fe}/\text{H}] < -5.3$), and SDSS J1742+2531 ($G_{\text{mag}} = 18.6$, $[\text{Fe}/\text{H}] = -4.8$) were discovered by Bonifacio et al. (2015, 2018b) and are CEMP stars too faint to be observed with ESPRESSO with a reasonable amount of time.
- SDSS J1029+1729 ($G_{\text{mag}} = 16.5$, $[\text{Fe}/\text{H}] = -4.73$, Caffau et al. 2011a), and Pristine_221.8781+9.7844 ($G_{\text{mag}} = 16.2$, $[\text{Fe}/\text{H}] = -4.66$, Starkenburg et al. 2018) show no CH absorptions and only an upper limit for carbon abundance have been provided. This carbon-normal population was out of the scope of this project.
- SDSS J0929+0238 ($G_{\text{mag}} = 17.9$, $[\text{Fe}/\text{H}] = -4.97$, Bonifacio et al. 2015) has been proved to be not a binary but a multiple CEMP system (Caffau et al. 2016).
- SDSS J0815+4729 ($G_{\text{mag}} = 16.7$, $[\text{Fe}/\text{H}] = -5.5$, Aguado et al. 2018b; González Hernández et al. 2020) is an extremely carbon enhanced star but not visible from Paranal.

We also note that for our 8 stars observed with ESPRESSO the Renormalised Unit Weight Error (RUWE) published by Gaia EDR3 Gaia Collaboration et al. (2021) is around 1 in all cases (See Table 3) and much below 1.4 anyway. Therefore, no binarity could be detected by means of RUWE data. In the following we show the results from our follow-up ESPRESSO observations of the other 7 CEMP-*no* stars with $[\text{Fe}/\text{H}] < -4.5$.

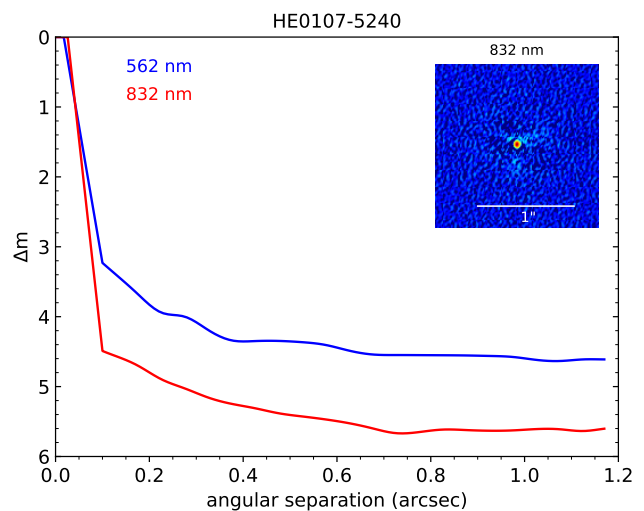


Fig. 6: The panel presents our final 5σ contrast curves, in 562 nm and 832 nm, that is the limiting magnitude reached in each filter as a function of angular distance from the diffraction limit out to 1.2 arcsec. The insets shows the 832 nm speckle interferometric reconstructed image in which the brighter primary component is at the center.

8.1. SDSS J0023+0307

Firstly reported by Aguado et al. (2018a) and subsequently observed at high-resolution (Aguado et al. 2019; Frebel et al. 2019), J0023–0307 is a $[\text{Fe}/\text{H}] < -6.1$ dwarf star with no iron lines detected yet. We visited J0023–0307 three times during Oct-Dec 2019 with approximately one month interval between observations done with the same setup. This star is faint ($G_{\text{mag}} = 17.6$) and therefore only the prominent Mg I b were marginally detected. Consequently, the CCF can be computed only with a synthetic template and the errors are large ($\sim 150 \text{ m s}^{-1}$). All the three v_{rad} measurements obtained with ESPRESSO are consistent with literature values (-195.5 ± 1.0 and $-194.6 \pm 1.2 \text{ km s}^{-1}$ for Aguado et al. (2019) and Frebel et al. (2019) respectively). Therefore no evidence for radial velocity variation is shown by the measurements. We report the ESPRESSO values in Table 2 but not including this object in Fig. 7 for clarity.

8.2. HE 0233–0343

This turn-off star with $[\text{Fe}/\text{H}] = -4.68$ (Hansen et al. 2014) and $G_{\text{mag}} = 15.3$ was observed four times between Aug-Oct 2019. The G-band around 4330\AA is detected in the ESPRESSO spectra and was used to cross-correlate with the natural template. As a result, the four observations with an average value of 52.107 km s^{-1} are compatible at 2σ . Hansen et al. (2014) reported $v_{\text{rad}} = 64 \text{ km s}^{-1}$ from high-resolution UVES data. To confirm this hint of variability we retrieved the UVES data from the ESO archive -program ID 69.D-0130(A). Following a similar approach to the ESPRESSO data, we derived from three UVES existing spectra $v_{\text{rad}} = 52.0 \pm 0.6$, 51.7 ± 0.6 , and $51.4 \pm 0.6 \text{ km s}^{-1}$ respectively. This completely agrees with the ESPRESSO measurements summarised in Table 2. We speculate that the measure of Hansen et al. (2014) does not account for the barycentric correction which is between $V_{\text{bar}} = -10.5$ and -12.0 km s^{-1} , that would explain the discrepancy. Further observation would be required to verify longer-term binarity.

8.3. SMSS 0313–6708

At the time of writing SMSS 0313–6708 is the most iron-poor star ever known with $[\text{Fe}/\text{H}] < -7.3$ and $G_{\text{mag}} = 14.5$. This target was visited 10 times in the period Aug 2019–Feb 2021. Three observations were repeated within the same night but removed from the v_{rad} series since is significantly lower quality than the other observations. The first group of data corresponding to 2019 seem consistent with no variation while the measurements in 2012 provide light hints of decreasing behaviour (See Table 7). All together, the measurements are consistent with no variation at 2σ but further observations could provide a more complete picture if were this star a large period binary system. The chemistry associated with these observations will be published in a separate article.

8.4. HE 0557–4840

Identified by Norris et al. (2007), this evolved UMP star with $[\text{Fe}/\text{H}] = -4.75$ and $G_{\text{mag}} = 15.2$ was observed with ESPRESSO in three different nights in the period Oct 2019–Jan 2020. Due the weakness of CH absorptions in the G-band, the CCF was built around the Mg I b region and the v_{rad} measurements are fully compatible with an average of 212.2 km s^{-1} (See Fig. 7). Other measurements from the bibliography included in Norris et al. (2007) and Arentsen et al. (2019) report a similar mean value though with larger error bars at the level of 1 km s^{-1} .

8.5. SDSS J1313–0019

SDSS J1313–0019, $G_{\text{mag}} = 16.4$, was discovered by Allende Prieto et al. (2015) and lately studied by Frebel et al. (2015) and Aguado et al. (2017). According to the high-resolution data from Mike at Magellan (Frebel et al. 2015), this evolved star is $[\text{Fe}/\text{H}] = -5.00$, highly carbon-enhanced $[\text{C}/\text{Fe}] = +3.0$, and shows $v_{\text{rad}} = 274.6 \text{ km s}^{-1}$ (no error bars were reported). We observed it just once in March 2022 -6 years later- giving as a result $v_{\text{rad}} = 273.98 \pm 0.05 \text{ km s}^{-1}$. The observed difference ($\sim 620 \text{ m s}^{-1}$) is clearly smaller than most optimistic uncertainty from Mike observations ($1 - 2 \text{ km s}^{-1}$). Furthermore, by cross matching this object with the *Survey of Surveys* database (Tsantaki et al. 2022), we found $v_{\text{rad}} = 273.054 \pm 4.498 \text{ km s}^{-1}$ from SEGUE data, in perfect agreement with those from high-resolution observations. There are, however, other measurements from low-resolution observations reported by Allende Prieto et al. (2015), $v_{\text{rad}} = 268 \pm 6 \text{ km s}^{-1}$ (July 2008, SEGUE), and $v_{\text{rad}} = 242 \pm 4 \text{ km s}^{-1}$ (March 2014, BOSS). While both SEGUE values are consistent with Mike and ESPRESSO data, the BOSS measurement (which is closer in time) seems to be incompatible. That fact allowed Allende Prieto et al. (2015) and Frebel et al. (2015) to suggest that SDSS J1313–0019 could be a binary system. However, the large uncertainty given by the low-resolution data and the fact that both high-resolution measurements are largely compatible do not allow us to claim for v_{rad} variability. Alternatively, the data in hand does not preclude completely some binarity behaviour, more ESPRESSO measurements are required.

8.6. HE 1327–2326

Firstly studied by Frebel et al. (2005), this HMP star with $[\text{Fe}/\text{H}] = -5.60$ and $G_{\text{mag}} = 13.4$ was observed 9 times between May 2019 and March 2022. Despite the observations span

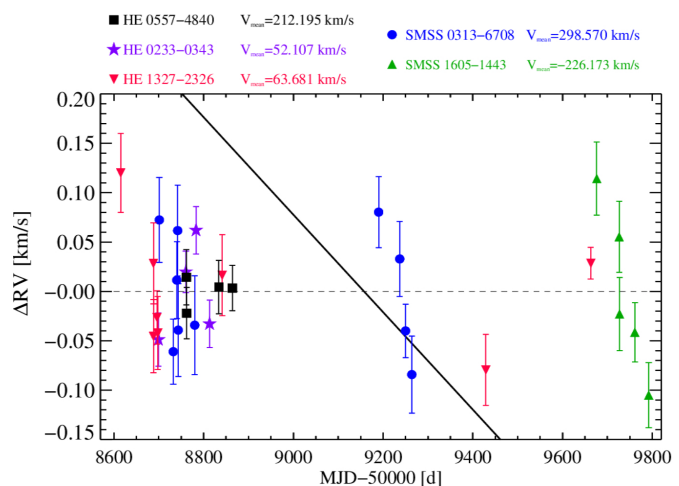


Fig. 7: A summary of the v_{rad} ESPRESSO measurements discussed in Section 8 in which the baseline is the average for each star for display purposes. The stars are shown with different colours and symbols: black square is HE 0557–4840 with a mean velocity taken at $212.195 \text{ km s}^{-1}$; violet stars is HE 0233–0343 with $(v_{\text{rad}})_{\text{mean}} = 52.107 \text{ km s}^{-1}$; red downwards triangles is HE 1327–2326 with $(v_{\text{rad}})_{\text{mean}} = 63.681 \text{ km s}^{-1}$; blue dots is SMSS 0313–6708 with $(v_{\text{rad}})_{\text{mean}} = 298.560 \text{ km s}^{-1}$; green upwards triangles SMSS 1605–1443 $(v_{\text{rad}})_{\text{mean}} = -226.173 \text{ km s}^{-1}$. Errors are of 1σ . For reference, the black line crossing the panel is the average variation of HE 0107–5240 in the same interval.

over three years no evidence of variability is found. The second observation (See Fig. 7) deviates from the main value by more than 2σ but the quality of this spectrum was much lower than the others due to poor observing conditions. As in the case of SMSS 0313–6708, the chemical analysis of the combined spectrum will be published separately in a forthcoming paper.

8.7. SMSS 1605–1443

SMSS 16054–1443 is a recent MMP halo giant discovered by Nordlander et al. (2019) with the SkyMapper telescope. With $G_{\text{mag}} = 15.4$ and a metallicity of $[\text{Fe}/\text{H}] = -6.2$ (1D-LTE), it is the lowest abundance of iron ever detected in a star. The star is strongly carbon-enhanced, $[\text{C}/\text{Fe}] = 3.9$, and has no significant s- or r-process enrichment, $[\text{Sr}/\text{Fe}] < 0.2$ and $[\text{Ba}/\text{Fe}] < 1.0$ being very likely a CEMP-*no* star. The authors in Nordlander et al. (2019) reported $v_{\text{rad}} = -224 \text{ km s}^{-1}$ from observations with Mike at Magellan telescope in September 2018, although no error bars were provided. Based in our experience, a reasonable uncertainty for that measurement could be of the order of $1 - 2 \text{ km s}^{-1}$. 43 months later we detected a $\sim 2 \text{ km s}^{-1}$ difference from 5 ESPRESSO measurements $(v_{\text{rad}})_{\text{mean}} = -226.173 \text{ km s}^{-1}$ (see Table 2). Therefore, we can expect a decrease rate of $\sim 1.6 \text{ m s}^{-1} \text{ d}^{-1}$. Our observations span $\sim 115 \text{ d}$ and show a decrease of $\sim 219 \text{ m s}^{-1}$ (see Fig. 7), giving a rate of approximately $\sim 1.9 \text{ m s}^{-1} \text{ d}^{-1}$ which is about consistent with the rate derived comparing Mike and ESPRESSO. We find this result convincing and tentatively propose that SMSS 16054–1443 could be another system similar to HE 0107–5240 but varying 3 times faster. More ESPRESSO observations are required to confirm this hypothesis and calculate orbital parameters.

9. Discussion

9.1. Binarity of our CEMP-*no* sample

We have probed 8 of the most extreme metal poor CEMP-*no* stars for binarity by means of very accurate radial velocity measurements obtained with ESPRESSO and we only found clear evidence for binarity only in the case of HE 0107–5240. For this star Suda et al. (2004) invoked mass transfer from a companion AGB in a similarly to what is believed to happen in CEMP-*s* stars (i.e., stars with $[\text{Ba}/\text{Fe}] > 1$). Moreover, Arentsen et al. (2019) suggested the presence of a radial velocity variation by comparison of the UVES observations with some observations taken at the High-Resolution Spectrograph (HRS) on the SALT Telescope. They noted that the radial velocity of HE 0107–5240 was almost 4 km s^{-1} larger than at the discovery time. On the basis of possible binarity Arentsen et al. (2019) suggested that the enhancement in Carbon could have been the result of mass transfer from the companion star. The period derived here for HE 0107–5240 is so long and the minimum mass of the companion so low that very unlikely there is any interaction or mass exchange between the two stars of the system. The result for HE 0107–5240 and for the other 7 stars is therefore quite consistent with the CEMP-*no* being either single or in binary systems with low mass companions as found by Hansen et al. (2016a,b) in a sample of more metal rich CEMP-*no* stars.

9.2. The stellar structure of HE 0107–5240

HE 0107–5240 lies in the position of the LRGB in the $T_{\text{eff}}\text{-log } g$ diagram (Mucciarelli et al. 2022), and has not experienced the mixing episode that occurs at the Red Giant Branch bump, and therefore the chemical composition is expected to be that of the natal cloud. Thus, the metallicity is so low that several or even just one SNe are enough to yield all the metals measured in the stellar atmospheres (Umeda & Nomoto 2003; Bonifacio et al. 2003; Limongi et al. 2003). The observed carbon abundances in CEMP-*no* stars is believed to come from faint supernovae of energy of 10^{51} erg, where fallback and mixing mechanisms played a role (Umeda & Nomoto 2003). Bonifacio et al. (2015) proposed an alternative explanation invoking double source: lighter elements, typically CNO, synthesised by faint SNe but heavier elements, some α 's included, by classical core-collapse SNe. For HE 0107–5240 we provide more stringent upper limits for the neutron capture elements and a first measure of the $^{12}\text{C}/^{13}\text{C}$. Hansen et al. (2015) found evidence of a *floor* in the absolute Ba abundance of CEMP-*no* stars at the abundance level of $A(\text{Ba}) \approx -2$. The existence of such a plateau was considered a specific feature of the CEMP-*no* stars and related to their progenitors. Both *spinstar* models (i.e., metal-poor stars rotating fast Meynet et al. 2006a; Choplin et al. 2018) and mixing and fall back models (Umeda & Nomoto 2003; Nomoto et al. 2013) predict the production of an important amount of neutron capture elements which apparently are not seen in HE 0107–5240. This is generally interpreted as a minimum amount of Ba produced by the *spinstars* (Cescutti et al. 2016). The present upper limit of $A(\text{Ba}) < -3.17$ derived here is more than an order of magnitude below the level of the suggested floor value and provides evidence of a much reduced n-capture element production by the early generation of stars.

9.3. The isotopic ratio $^{12}\text{C}/^{13}\text{C}$

In HE 0107–5240 we have been able to measure the $^{12}\text{C}/^{13}\text{C}$ ratio. ^{12}C is a primary product of stellar nucleosynthesis and is formed in the triple- α process during hydrostatic helium burning. The stable ^{13}C isotope is produced in the hydrogen-burning shell when the CN-cycle converts ^{12}C into ^{13}C . These processes, which occur mainly in intermediate massive stars which develop as AGB (Wannier 1980), lead to a CN-cycle equilibrium ratio of about $^{12}\text{C}/^{13}\text{C} \approx 3.4$. Large quantities of ^{13}C could also be produced by low-metallicity massive and fast-rotating stars which should mostly affect the early chemical evolution (Meynet et al. 2006b; Limongi & Chieffi 2018; Maeder et al. 2015). Meynet et al. (2006b) showed that the isotope composition in the stellar wind is characterised by very low values of $^{12}\text{C}/^{13}\text{C} \sim 3 - 5$. Due to the contribution of relatively long-lived stars the chemical evolution models of the Galaxy predict a decrease of the isotopic ratio $^{12}\text{C}/^{13}\text{C}$ with time, and an increase with galactocentric distances (Romano & Matteucci 2003). In fact, the photospheric solar ratio $^{12}\text{C}/^{13}\text{C} = 95 \pm 5$ (Asplund et al. 2006) is higher than the value found in local molecular clouds ($^{12}\text{C}/^{13}\text{C} \sim 60 - 70$, Goto et al. 2003; Milam et al. 2005), and is significantly higher than the at measured in the Galactic Center by Wilson & Matteucci (1992), $^{12}\text{C}/^{13}\text{C} = 25 \pm 5$.

At high redshift, carbon abundance had been measured in the metal-poor damped Ly α systems (DLA). Welsh et al. (2020) reported a bound on the carbon isotope ratio $^{12}\text{C}/^{13}\text{C} > 2.3$ (2σ) in a DLA system at $z = 2.34$. They found also tentative evidence that the *most* metal-poor DLA population exhibits somewhat higher $[\text{C}/\text{O}]$ values at redshift $z \lesssim 3$ with a potential upward trend in the ratio going towards lower redshift. They argued that the elevated $[\text{C}/\text{O}]$ ratios at $z \lesssim 3$ might be a signature of enrichment from the first metal-enriched low- and intermediate-mass stars. At somewhat lower redshift there are few determinations of the carbon isotopic ratio. Muller et al. (2006) obtained a $^{12}\text{C}/^{13}\text{C}$ ratio of 27 ± 2 in the Galaxy at $z_{\text{abs}} = 0.89$ by using the C I transitions. Levshakov et al. (2006) obtained $^{12}\text{C}/^{13}\text{C} > 80$ in the $z_{\text{abs}} = 1.15$ DLA towards HE 0515–4414 implying a very low ^{13}C abundance. Carswell et al. (2011) in the $z_{\text{abs}} = 1.7764$ DLA system toward J1331 + 170, which is also the system we are studying here by means of new ESPRESSO observations, derived $^{12}\text{C}/^{13}\text{C} > 5$ (2σ).

Hansen et al. (2015); Norris et al. (2013) measured the $^{12}\text{C}/^{13}\text{C}$ in a sample of CEMP stars. Most of them have low $^{12}\text{C}/^{13}\text{C}$ as a result of high ^{13}C , but they also show $[\text{C}/\text{N}] < 0$ which is evidence of internal mixing according to Spite et al. (2006). HE 0107–5240 shows $[\text{C}/\text{N}] > 0$ and therefore is unmixed. Consequently, the new measure of $^{12}\text{C}/^{13}\text{C} = 87 \pm 6$ implies that the low ^{13}C is pristine. This suggests that the parent generation of stars that polluted the material from which this star is born did not produce any significant amount of ^{13}C . *Spinstar* models (Meynet et al. 2006a), which predict production of an important amount of ^{13}C , are therefore not favoured.

9.4. The lithium during the HE 0107–5240 evolution

The upper limit of Li in HE 0107–5240 is also improved with $A(\text{Li}) < 0.5$ with a confidence level higher than 3σ . HE 0107–5240 is in the lower red giant branch, LRGB, namely stars with $2 \leq \log g \leq 3$ located after the first dredge-up (FDU) and before the RGB-bump luminosity. Assuming these stars start with the same initial Li abundance, the present Li abundance depends on how much Li has been destroyed in the extension of the convection zone during the FDU. Mucciarelli et al. (2022)

found that the majority of LRGB show a very thin plateau in the Li abundance with $A(\text{Li}) = 1.09 \pm 0.07$ and that this results from the stellar dilution in the giant evolution. They also found that a small fraction of stars of about 20% shows no detectable Li, namely $A(\text{Li}) \leq 0.7$. For HE 0107–5240 Mucciarelli et al. (2022) derived $A(\text{Li}) \leq 0.7$ which we improve slightly in $A(\text{Li}) \leq 0.5$. This bound places HE 0107–5240 in the minority of stars without any Li signature. Another LRGB we are investigating for radial velocity changes, HE 0557–4840, shows also absence of Li with $A(\text{Li}) < 0.60$ (Mucciarelli et al. 2022). It is not clear for these stars if they were originally Li poor objects or if they suffered from extra destruction of Li either during the main sequence or the post-main sequence evolution. However, this seems uncorrelated with metallicity since Li has been measured at $A(\text{Li}) = 0.87 \pm 0.05$ also in SMSS J0313–6708 which, with $[\text{Fe}/\text{H}] < -7.0$, is the lowest metallicity star known and, therefore, a similar abundance is expected also in the other more metal rich subgiants. Since theoretically there is no known mechanism that can destroy Li in the MS or in the RGB before the RGB-bump, there are three main scenarios left to explain the metal-poor CEMP-*no* stars with no or low Li detection:

1. The gas from which the star was formed was Li-free. This may be the case if the star was formed from almost pure SN ejecta, with very little dilution by primordial gas.
2. Li was destroyed in the pre-main sequence phase (Fu et al. 2015). This phase is not easily modelled and the question remains in what the pre-MS of these stars was different, with respect to that of other stars that retained Li. In Fu et al. (2015) the model of the resulting Li is a balance between a pre-main sequence destruction and partial accretion of gas with Li at the primordial value. In general, these stars less massive for a given T_{eff} and such a balance could have been broken.
3. The star is an evolved Blue Straggler. Ryan et al. (2001) suggested that unevolved metal-poor stars with no detectable Li were “Blue Stragglers-to-be”, and in fact the Gaia parallaxes have shown that three out of four stars studied by Ryan et al. (2001) are indeed “canonical” Blue Stragglers (Bonifacio et al. 2018a). If this were true in the case of HE 0107–5240, we should postulate that the system was initially a hierarchical triple system with an inner pair that eventually coalesced to form a Blue Straggler and an outer companion that is the companion presently revealed by the orbital motion.

Bonifacio et al. (2018b) and Aguado et al. (2019) studied several dwarf stars with extremely low metallicity, and only 3 out of 8 dwarfs with $[\text{Fe}/\text{H}] < -4.2$ have detectable Li close to, but below, the Spite plateau. It is therefore very likely that the high fraction of Li-depleted stars is related to the significant Li destruction by the progenitor responsible for the high carbon abundances observed in the CEMP-*no* stars.

9.5. Consequences on the nature of CEMP-*no* stars

The lack of binaries among the CEMP-*no* stars holds important bearings on the star formation of stars from primordial or nearly primordial chemistry. At the time of the discovery of HE 0107–5240, the possibility to form a low mass star from almost metal-free gas was not conceived (Palla 2003). In the conventional model of primordial star formation H_2 cooling of metal-free gas leads to the formation of massive stars with a characteristic stellar mass of $\approx 100 M_{\odot}$.

The discovery of the extremely metal poor CEMP-*no* stars led to a revision of the processes for the formation of low-mass

stars. Bromm & Loeb (2003) suggested that atomic lines of neutral oxygen and singly ionised carbon could effectively cool a very metal-poor contracting cloud, provided the abundance of these elements is at the level observed in the CEMP stars. However, the successive discovery of two extremely metal poor stars which are not carbon enhanced (Caffau et al. 2011a; Starkenburg et al. 2018) suggests that metal-line cooling cannot be the only mechanism capable of leading the formation of a sub-solar mass at very low metallicity. Smaller masses of the order of $1 M_{\odot}$ may only be obtained by dust cooling. However, recent refinements in the modelling of the collapse process of primordial star formation have shown that the original clouds are prone to fragmentation (Greif 2015). This leads more likely to the formation of a massive central star or a binary system surrounded by some small mass stars. In the simulation of Becerra et al. (2015) of a cooling primordial cloud, they found that the fragmentation of the disc around the initial protostar could generate a second protostellar system with 5–10 members with mass of the order of the $1 M_{\odot}$. They also showed that at the end of the simulation the collapse could evolve into a wide binary system with a distance of hundreds of AU. The confirmation of the binarity of HE 0107–5240, which is one of the most metal-poor stars known, shows that the process of star formation in very metal-poor gas could lead to the formation of binaries. However, the majority of single stars show that probably these initial clusters dispersed or did not end up preferentially into binary systems.

10. Conclusions

We summarise here the main conclusions:

- Along the time span of 3 years we observed 8 of the most metal poor CEMP-*no* stars with ESPRESSO to probe binarity by means of very accurate radial velocities.
- Out of these, only HE 0107–5240 showed clear evidence for an orbital motion. HE 0107–5240 shows a monotonic decreasing trend in radial velocity at a rate of approximately $0.5 \text{ m s}^{-1} \text{ d}^{-1}$. The maximum v_{rad} was reached between Mar 13th, 2012 and Dec 8th, 2014 and the period is constrained at $P_{\text{orb}} = 13009^{+1496}_{-1370} \text{ d}$. The v_{rad} for other 6 EMP CEMP-*no* stars are consistent with single stars while solid indication of binarity behaviour in SMSS 1605–1443 with an approximate v_{rad} variation of $\sim 1.6 \text{ m s}^{-1} \text{ d}^{-1}$ are found.
- Speckle observations of HE 0107–5240 do not reveal companions at distances greater than 1000 AU.
- Revised Chemistry of HE 0107–5240 provided more stringent upper limits to $[\text{Sr}/\text{Fe}] < -0.76$ and $[\text{Ba}/\text{Fe}] < +0.20$ confirming the star is a CEMP-*no*. The isotopic ratio $^{12}\text{C}/^{13}\text{C}$ is measured for the first time in an unmixed giant and found close to the solar value. The low ^{13}C is in contrast to what is expected from a *spinstar* progenitor. Lithium is also improved to a value of $A(\text{Li}) < 0.5$ well below the Li plateau at 1.1 found in the Lower Red Giant Branch Stars by Mucciarelli et al. (2022), suggesting the star was originally depleted by lithium.
- The fact that there are some binaries among the CEMP-*no* group (HE 0107–5240, SDSS J0929+0238, and likely SMSS 1605–1443) indicates that the low metallicity does not inhibit the formation of binaries.

Acknowledgements. The authors wish to thank the Gemini Director for the allocation of engineering time to perform this observation. DA would like to thank Dr. Megan Bedell for her enjoyable discussion of the ESPRESSO data at the Flatiron Institute. DA also acknowledges support from the ERC Starting Grant NEFERTITI H2020/808240. JIGH, CAP, ASM and RR acknowledge financial support from the Spanish Ministry of Science and Innovation

(MICINN) project PID2020-117493GB-I00. JIGH also acknowledges financial support from the Spanish MICINN under 2013 Ramón y Cajal program RYC-2013-14875. A. S. M. acknowledges financial support from the Spanish Ministry of Science and Innovation (MICINN) under 2018 Juan de la Cierva program IJC2018-035229-I. Zorro was funded by the NASA Exoplanet Exploration Program and built at the NASA Ames Research Center by Steve B. Howell, Nic Scott, Elliott P. Horch, and Emmett Quigley. Gemini Observatory is a program of NSF's NOIRLab, which is managed by the Association of Universities for Research in Astronomy (AURA) under a cooperative agreement with the National Science Foundation, on behalf of the Gemini partnership: the National Science Foundation (United States), National Research Council (Canada), Agencia Nacional de Investigación y Desarrollo (Chile), Ministerio de Ciencia, Tecnología e Innovación (Argentina), Ministério da Ciência, Tecnologia, Inovações e Comunicações (Brazil), and Korea Astronomy and Space Science Institute (Republic of Korea). This work was supported by FCT - Fundação para a Ciência e a Tecnologia through national funds and by FEDER through COMPETE2020 - Programa Operacional Competitividade e Internacionalização by these grants: UID/FIS/04434/2019; UIDB/04434/2020; UIDP/04434/2020; PTDC/FIS-AST/32113/2017 & POCI-01-0145-FEDER-032113. CJM also acknowledges FCT and POCH/FSE (EC) support through Investigador FCT Contract 2021.01214.CEECIND/CP1658/CT0001. This work has made use of data from the European Space Agency (ESA) mission *Gaia* (<https://www.cosmos.esa.int/gaia>), processed by the *Gaia* Data Processing and Analysis Consortium (DPAC, <https://www.cosmos.esa.int/web/gaia/dpac/consortium>). Funding for the DPAC has been provided by national institutions, in particular the institutions participating in the *Gaia* Multilateral Agreement. This work was financed by FEDER-Fundo Europeo de Desenvolvimento Regional funds through the COMPETE 2020-Operational Programme for Competitiveness and Internationalisation (POCI), and by Portuguese funds through FCT - Fundação para a Ciência e a Tecnologia under projects POCI-01-0145-FEDER-028987, PTDC/FIS-AST/28987/2017, PTDC/FIS-AST/0054/2021 and EXPL/FIS-AST/1368/2021, as well as UIDB/04434/2020 & UIDP/04434/2020, CERN/FIS-PAR/0037/2019, PTDC/FIS-OUT/29048/2017. FPE and CLO would like to acknowledge the Swiss National Science Foundation (SNSF) for supporting research with ESPRESSO through the SNSF grants nr. 140649, 152721, 166227 and 184618. The ESPRESSO Instrument Project was partially funded through SNSF's FLARE Programme for large infrastructures. MTM acknowledges the support of the Australian Research Council through Future Fellowship grant FT180100194

References

- Aguado, D. S., Allende Prieto, C., González Hernández, J. I., & Rebolo, R. 2018a, *ApJ*, 854, L34
- Aguado, D. S., Allende Prieto, C., González Hernández, J. I., Rebolo, R., & Caffau, E. 2017, *A&A*, 604, A9
- Aguado, D. S., González Hernández, J. I., Allende Prieto, C., & Rebolo, R. 2018b, *ApJL*, 852, L20
- Aguado, D. S., González Hernández, J. I., Allende Prieto, C., & Rebolo, R. 2019, *ApJ*, 874, L21
- Allende Prieto, C., Fernández-Alvar, E., Aguado, D. S., et al. 2015, *A&A*, 579, A98
- Arentsen, A., Starckburg, E., Shetrone, M. D., et al. 2019, *A&A*, 621, A108
- Asplund, M., Grevesse, N., & Jacques Sauval, A. 2006, *Nucl. Phys. A*, 777, 1
- Barentsen, G., Hedges, C., Vinicius, Z., et al. 2021, *lightkurve/lightkurve: Lightkurve v2.0.9*, Zenodo
- Becerra, F., Greif, T. H., Springel, V., & Hernquist, L. E. 2015, *MNRAS*, 446, 2380
- Beers, T. C. & Christlieb, N. 2005, *Highlights of Astronomy*, 13, 579
- Bianchi, L., Herald, J., Efremova, B., et al. 2011, *Ap&SS*, 335, 161
- Bonifacio, P., Caffau, E., Spite, M., et al. 2015, *A&A*, 579, A28
- Bonifacio, P., Caffau, E., Spite, M., et al. 2018a, *Research Notes of the American Astronomical Society*, 2, 19
- Bonifacio, P., Caffau, E., Spite, M., et al. 2018b, *A&A*, 612, A65
- Bonifacio, P., Limongi, M., & Chieffi, A. 2003, *Nature*, 422, 834
- Bonifacio, P., Molaro, P., Adibekyan, V., et al. 2020, *A&A*, 633, A129
- Bonifacio, P., Molaro, P., Beers, T. C., & Vladilo, G. 1998, *A&A*, 332, 672
- Bromm, V. & Loeb, A. 2003, *Nature*, 425, 812
- Caffau, E., Bonifacio, P., François, P., et al. 2011a, *Nature*, 477, 67
- Caffau, E., Bonifacio, P., Spite, M., et al. 2016, *A&A*, 595, L6
- Caffau, E., Ludwig, H. G., Steffen, M., Freytag, B., & Bonifacio, P. 2011b, *Sol. Phys.*, 268, 255
- Carswell, R. F., Jorgenson, R. A., Wolfe, A. M., & Murphy, M. T. 2011, *MNRAS*, 411, 2319
- Cayrel, R. 2005, *Nature*, 434, 838
- Ceillier, T., Tayar, J., Mathur, S., et al. 2017, *A&A*, 605, A111
- Cescutti, G., Valentini, M., François, P., et al. 2016, *A&A*, 595, A91
- Chiaki, G., Tominaga, N., & Nozawa, T. 2017, *MNRAS*, 472, L115
- Choplin, A., Hirschi, R., Meynet, G., et al. 2018, *A&A*, 618, A133
- Christlieb, N., Bessell, M. S., Beers, T. C., et al. 2002a, *Nature*, 419, 904
- Christlieb, N., Green, P. J., Wisotzki, L., & Reimers, D. 2001, *A&A*, 375, 366
- Christlieb, N., Gustafsson, B., Korn, A. J., et al. 2004, *ApJ*, 603, 708
- Christlieb, N., Wisotzki, L., & Graßhoff, G. 2002b, *A&A*, 391, 397
- Collet, R., Asplund, M., & Trampedach, R. 2006, *ApJ*, 644, L121
- Creevey, O., Grundahl, F., Thévenin, F., et al. 2019, *A&A*, 625, A33
- Foreman-Mackey, D., Agol, E., Angus, R., & Ambikasaran, S. 2017, *ArXiv*
- Frebel, A., Aoki, W., Christlieb, N., et al. 2005, *Nature*, 434, 871
- Frebel, A., Chiti, A., Ji, A. P., Jacobson, H. R., & Placco, V. M. 2015, *ApJ*, 810, L27
- Frebel, A., Ji, A. P., Ezzeddine, R., et al. 2019, *ApJ*, 871, 146
- Fu, X., Bressan, A., Molaro, P., & Marigo, P. 2015, *MNRAS*, 452, 3256
- Fulton, B. J., Petigura, E. A., Blunt, S., & Sinukoff, E. 2018, *PASP*, 130, 044504
- Gaia Collaboration, Brown, A. G. A., Vallenari, A., et al. 2021, *A&A*, 649, A1
- González Hernández, J. I., Aguado, D. S., Allende Prieto, C., Burgasser, A. J., & Rebolo, R. 2020, *ApJ*, 889, L13
- Goto, M., Usuda, T., Takato, N., et al. 2003, *ApJ*, 598, 1038
- Greif, T. H. 2015, *Computational Astrophysics and Cosmology*, 2, 3
- Greif, T. H., Bromm, V., Clark, P. C., et al. 2012, *MNRAS*, 424, 399
- Hansen, C. J., Nordström, B., Hansen, T. T., et al. 2016a, *A&A*, 588, A37
- Hansen, T., Hansen, C. J., Christlieb, N., et al. 2015, *ApJ*, 807, 173
- Hansen, T., Hansen, C. J., Christlieb, N., et al. 2014, *ApJ*, 787, 162
- Hansen, T. T., Andersen, J., Nordström, B., et al. 2016b, *A&A*, 586, A160
- Howell, S. B., Everett, M. E., Sherry, W., Horch, E., & Ciardi, D. R. 2011, *AJ*, 142, 19
- Howell, S. B. & Furlan, E. 2022, *Frontiers in Astronomy and Space Sciences*, 9, 871163
- Jofré, P., Heiter, U., Soubiran, C., et al. 2014, *A&A*, 564, A133
- Johnson, J. L. & Li, H. 2012, *ApJ*, 751, 81
- Keller, S. C., Bessell, M. S., Frebel, A., et al. 2014, *Nature*, 506, 463
- Kurucz, R. L. 2005, *Memorie della Societa Astronomica Italiana Supplementi*, 8, 14
- Levshakov, S. A., Centurión, M., Molaro, P., & Kostina, M. V. 2006, *A&A*, 447, L21
- Limongi, M. & Chieffi, A. 2018, *ApJS*, 237, 13
- Limongi, M., Chieffi, A., & Bonifacio, P. 2003, *ApJ*, 594, L123
- Lodders, K. 2019, in *Nuclei in the Cosmos XV*, Vol. 219, 165–170
- Maeder, A., Meynet, G., & Chiappini, C. 2015, *A&A*, 576, A56
- Marconi, M., Musella, I., Fiorentino, G., et al. 2010, *ApJ*, 713, 615
- Meynet, G., Ekström, S., & Maeder, A. 2006a, *A&A*, 447, 623
- Meynet, G., Ekström, S., & Maeder, A. 2006b, *A&A*, 447, 623
- Milam, S. N., Savage, C., Brewster, M. A., Ziurys, L. M., & Wyckoff, S. 2005, *ApJ*, 634, 1126
- Mucciarelli, A., Monaco, L., Bonifacio, P., et al. 2022, *arXiv e-prints*, arXiv:2203.10347
- Muller, S., Guélin, M., Dumke, M., Lucas, R., & Combes, F. 2006, *A&A*, 458, 417
- Nomoto, K., Kobayashi, C., & Tominaga, N. 2013, *ARA&A*, 51, 457
- Nordlander, T., Bessell, M. S., Da Costa, G. S., et al. 2019, *MNRAS*, 488, L109
- Norris, J. E., Christlieb, N., Korn, A. J., et al. 2007, *ApJ*, 670, 774
- Norris, J. E., Ryan, S. G., & Beers, T. C. 1997, *ApJ*, 489, L169
- Norris, J. E., Yong, D., Bessell, M. S., et al. 2013, *ApJ*, 762, 28
- Palla, F. 2003, *Memorie della Societa Astronomica Italiana Supplementi*, 3, 52
- Pepe, F., Cristiani, S., Rebolo, R., et al. 2021, *A&A*, 645, A96
- Pepe, F., Cristiani, S., Rebolo, R., et al. 2013, *The Messenger*, 153, 6
- Preston, G. W. & Snenen, C. 2001, *AJ*, 122, 1545
- Ricker, G. R., Winn, J. N., Vanderspek, R., et al. 2015, *Journal of Astronomical Telescopes, Instruments, and Systems*, 1, 014003
- Romano, D. & Matteucci, F. 2003, *MNRAS*, 342, 185
- Ryan, S. G., Beers, T. C., Kajino, T., & Rosolankova, K. 2001, *ApJ*, 547, 231
- Sbordone, L. 2005, *Memorie della Societa Astronomica Italiana Supplementi*, 8, 61
- Scargle, J. D. 1982, *ApJ*, 263, 835
- Schneider, R., Ferrara, A., Salvaterra, R., Omukai, K., & Bromm, V. 2003, *Nature*, 422, 869
- Schneider, R., Omukai, K., Bianchi, S., & Valiante, R. 2012, *MNRAS*, 419, 1566
- Scott, N. J., Howell, S. B., Gnlika, C. L., et al. 2021, *Frontiers in Astronomy and Space Sciences*, 8, 138
- Speagle, J. S. 2020, *MNRAS*, 493, 3132
- Spite, M., Caffau, E., Bonifacio, P., et al. 2013, *A&A*, 552, A107
- Spite, M., Cayrel, R., Hill, V., et al. 2006, *A&A*, 455, 291
- Starkenburg, E., Aguado, D. S., Bonifacio, P., et al. 2018, *MNRAS*, 481, 3838
- Suda, T., Aikawa, M., Machida, M. N., Fujimoto, M. Y., & Iben, Icko, J. 2004, *ApJ*, 611, 476
- Tauris, T. M. & van den Heuvel, E. P. J. 2006, in *Compact stellar X-ray sources*, Vol. 39, 623–665

- Tody, D. 1993, in *Astronomical Society of the Pacific Conference Series*, Vol. 52, *Astronomical Data Analysis Software and Systems II*, ed. R. J. Hanisch, R. J. V. Brissenden, & J. Barnes, 173
- Tonry, J. & Davis, M. 1979, *AJ*, 84, 1511
- Tsantaki, M., Pancino, E., Marrese, P., et al. 2022, *A&A*, 659, A95
- Umeda, H. & Nomoto, K. 2003, *Nature*, 422, 871
- Venn, K. A., Puzia, T. H., Divell, M., et al. 2014, *ApJ*, 791, 98
- Wannier, P. G. 1980, *ARA&A*, 18, 399
- Welsh, L., Cooke, R., Fumagalli, M., & Pettini, M. 2020, *MNRAS*, 494, 1411
- Wilson, T. L. & Matteucci, F. 1992, *A&A Rev.*, 4, 1
- Yoon, J., Beers, T. C., Placco, V. M., et al. 2016, *ApJ*, 833, 20
- Yoon, J., Beers, T. C., Tian, D., & Whitten, D. D. 2019, *ApJ*, 878, 97
- Zechmeister, M. & Kürster, M. 2009, *A&A*, 496, 577

-
- ¹ Dipartimento di Fisica e Astronomia, Università degli Studi di Firenze, Via G. Sansone 1, I-50019 Sesto Fiorentino, Italy.
- ² INAF-Osservatorio Astrofisico di Arcetri, Largo E. Fermi 5, I-50125 Firenze, Italy.
- ³ INAF-Osservatorio Astronomico di Trieste, Via G.B. Tiepolo 11, I-34143 Trieste, Italy.
- ⁴ Institute of Fundamental Physics of the Universe, Via Beirut 2, Miramare, Trieste, Italy.
- ⁵ GEPI, Observatoire de Paris, Université PSL, CNRS, 5 Place Jules Janssen, 92190 Meudon, France.
- ⁶ Instituto de Astrofísica de Canarias, Vía Láctea, 38205 La Laguna, Tenerife, Spain.
- ⁷ Universidad de La Laguna, Departamento de Astrofísica, 38206 La Laguna, Tenerife, Spain.
- ⁸ Centro de Astrobiología (CSIC-INTA), Carretera Ajalvir km 4, 28850 Torrejón de Ardoz, Madrid, Spain.
- ⁹ Consejo Superior de Investigaciones Científicas, 28006 Madrid, Spain.
- ¹⁰ INAF - Osservatorio Astrofisico di Torino, Via Osservatorio 20, I-10025 Pino Torinese, Italy.
- ¹¹ NASA Ames Research Center, Moffett Field, CA 94035, USA.
- ¹² NASA Exoplanet Science Institute, Caltech/IPAC, Mail Code 100-22, 1200 E. California Blvd., Pasadena, CA 91125, USA.
- ¹³ Scuola Normale Superiore Piazza dei Cavalieri, 7 I-56126 Pisa.
- ¹⁴ Instituto de Astrofísica e Ciências do Espaço, Faculdade de Ciências da Universidade de Lisboa, Campo Grande, PT1749-016 Lisboa, Portugal.
- ¹⁵ Instituto de Astrofísica e Ciências do Espaço, CAUP, Universidade do Porto, Rua das Estrelas, 4150-762, Porto, Portugal.
- ¹⁶ Centro de Astrofísica da Universidade do Porto, Rua das Estrelas, 4150-762 Porto, Portugal.
- ¹⁷ European Southern Observatory, Karl-Schwarzschild-Str. 2, 85748 Garching bei München, Germany.
- ¹⁸ Centre for Astrophysics and Supercomputing, Swinburne University of Technology, Hawthorn, Victoria 3122, Australia.
- ¹⁹ Observatoire Astronomique de l'Université de Genève, Chemin Pégasi 51, Sauverny 1290, Switzerland
- ²⁰ Département d'astronomie de l'Université de Genève, Chemin Pégasi 51, 1290 Versoix, Switzerland.
- ²¹ Instituto de Astrofísica e Ciências do Espaço, CAUP, Universidade do Porto, Rua das Estrelas, 4150-762 Porto, Portugal.
- ²² Departamento de Física e Astronomia, Faculdade de Ciências, Universidade do Porto, Rua Campo Alegre, 4169-007 Porto, Portugal.